Exploring Stress-Induced Neural Circuit Remodeling through Data-Driven Analysis and Artificial Neural Network Simulation

Feng Lin *[a]

[a] *Institute of blood transfusion, Chinese academy of medical science and Peking union medical college, No.26 Huacai Road, Chengdu, 610052, People's Republic of China*

ABSTRACT: Chronic stress induces behavioral rigidity and neural circuit remodeling, yet the underlying computational mechanisms remain unclear. In this study, we analyze in vivo GCaMP8s recordings from the amygdala-striatal circuits (Giovanniello et al.) and identify a difference in the recovery dynamics of the BLA-DMS and CeA-DMS pathways following acute perturbations. Through data analysis and artificial neural network modeling, we find that structural asymmetry and functional separation–formalized by distinct optimization objectives–are necessary for simulating the experimental results. This suggests that the divergent functions of the BLA-DMS (exploration/precision) and CeA-DMS (stabilization/homeostasis) pathways are inherent, not learned. Under chronic stress, the brain adapts by strengthening the CeA-DMS pathway's stabilizing role. A robustness test (10 independent seeds) confirmed the statistical reliability of the results (e.g., Recovery Time difference), yet revealed a high Coefficient of Variation in pathway coupling weights ($\approx 40\%$), suggesting the brain preserves structural flexibility even while enforcing rigid functional outcomes. The model replicates the observed outcomes, suggesting that the chronic stress is computationally equivalent to a gain shift favoring the stable CeA-DMS pathway.

KEYWORDS: Amygdala-Striatal Circuits; Chronic Stress; Artificial Neural Network Simulation; Cognitive Neuroscience; Data-Driven Modeling

1 Introduction

Establishing a precise mapping between psychological states and their underlying neural substrates remains a central tenet of cognitive neuroscience [1]. Psychological processes are rooted in the dynamics of specific neural circuits. In this view, external behavioral patterns serve as direct readouts of internal neural computations [2]. By quantitatively analyzing the neural signals associated with these behaviors, it becomes possible to reverse-engineer the brain's operational logic and computational strategies across various psychological states [3]. Furthermore, this mind-brain-behavior relationship is inherently dynamic: environmental factors and constraints often drive shifts in psychological states, triggering a modulation of neural circuits that results in adaptive behavioral changes.

This dynamic mapping is evident in the context of stress, a potent environmental constraint that precipitates significant shifts in both psychological states and behavioral strategies [4]. Specifically, exposure to chronic stress has been observed to induce a transition from flexible, goal-directed behaviors to rigid, habitual patterns (often referred to as "behavioral rigidity") [5]. From a psychological perspective, this shift represents an adaptive "mindset" change aiming for efficiency and robustness under uncertainty. Crucially, neurophysiological research has grounded this shift in the reorganization of dual amygdala-striatal

---

*E-mail: linfeng@ibt.pumc.edu.cn

pathways: prolonged chronic stress attenuates the goal-directed basolateral amygdala (BLA) to dorsomedial striatum (DMS) pathway, while progressively recruiting the central amygdala (CeA) to DMS pathway, a reconfiguration that directly promotes the formation of inflexible habits.

From the perspective of complex systems theory, the brain operates as a dynamic entity capable of maintaining external stability against perturbations (such as noise) while retaining the internal plasticity required to adapt to changing environments [6,7]. These characteristics–coexisting stability and flexibility–imply that the brain exhibits chaotic dynamics [8]. In parallel, the brain can be conceptualize as a highly plastic learning system, where synaptic weights are continuously updated in response to external stimuli or training, which is in accordance with artificial neural networks (ANNs) [9–12]. In the light of this view, the experimental designs of Giovanniello et al. [5], the chronic stress environment effectively functioned as a specific "training set." The mice were not merely exposed to stress; rather, their neural networks were "trained" by these high-pressure environmental statistics, which consequently reshaped their underlying neural circuitry.

Despite demonstrating a causal link between chronic stress, pathway signal alterations, and behavioral rigidity, the precise computational mechanisms–specifically how these signals dynamically reconfigure neural circuits at the network level–remain unclear. Traditional methods, such as direct signal observation and behavioral analysis, do not capture the full complexity of this reorganization, thus limiting our understanding of its underlying logic. To address this gap, this study leverages the GCaMP8s fluorescence time-series data disclosed by their work. We first analyze these data to extract key statistical and dynamical characteristics, which serve as physical constraints for our model construction. To explore these mechanisms, we construct a Unified Coupled System (UCS) based on artificial neural networks (ANNs), which enables the simulation of neural circuit dynamics and provides a robust platform for understanding how chronic stress might influence neural reorganization and behavioral shifts. By verifying whether the UCS can spontaneously reproduce the observed biological phenomena, we aim to provide a mechanistic explanation for how the brain optimizes its working strategy under environmental stress.

2 Method

2.1 Data Source

We performed a secondary analysis on the experimental data originally reported by Giovanniello et al. [5]. The dataset comprises GCaMP8s fiber photometry recordings (sampling rate: 20 Hz) extracted from time windows of ±10s aligned to specific behavioral events, including bout-initiating presses, reward collection, non-contingent rewards, and footshock. Signals were recorded from neurons in the basolateral amygdala (BLA) and central amygdala (CeA) projecting to the dorsomedial striatum (DMS). The original experiments utilized wild-type C57BL/6J mice. Notably, based on an average murine lifespan of 26-30 months [13], the 14-day chronic stress exposure corresponds to approximately 1.5-2.0% of the lifespan. This duration is translationally equivalent to 1.2-1.4 years of chronic stress in humans. This provides a robust temporal window for examining stress-induced neural plasticity. We categorized experimental stimuli into two main types: non-contingent stimuli (footshock, unpredicted reward) and contingent instrumental behaviors (bout-initiating press, contingent reward), based on their contingency and prior training context.

To investigate the neural dynamics under varying degrees of agency, predictability, and valence, we categorized the experimental stimuli and behaviors into distinct modalities defined by their instrumental contingency and prior training context.

1. Non-Contingent Stimuli. These stimuli are delivered independently of the mouse's current action, but differ critically by valence and exposure history. Aversive Stressor (Footshock): This represents a high-impact, purely aversive stimulus that occurs outside the instrumental learning context (i.e., not contingent on lever pressing). The stress cohort was subjected to repeated footshocks during the 14-day chronic stress paradigm, whereas the control group had minimal prior exposure. This stimulus is unique in its capacity

to trigger a non-instrumental, high-arousal defense mechanism. Appetitive Unpredicted Reward: These rewards are delivered non-contingently (timing is unpredictable), but they are appetitive and occur within a context where mice have established strong food-seeking associations through prior training. Thus, the uncertainty is confined to the timing of the outcome, rather than the existence of the food-reward association itself.

2. Contingent Instrumental Behaviors. These behaviors are purposeful and represent goal-directed actions within a learned context: Bout-Initiating Press and Contingent Reward. These focus on the animal's volitional action (the press) and the subsequent anticipated outcome (the contingent reward). The mice learned this association during training sessions. Crucially, the original study modulated the uncertainty of these outcomes using a Random Ratio (RR) schedule, progressively decreasing the probability of receiving a reward from 1.0 to 0.1 across sessions. This design created a gradient of increasing outcome uncertainty while strictly maintaining the animal's active agency and the learned instrumental contingency.

2.2 Data analysis

2.2.1 Statistical Perspective

To investigate the dynamic response and recovery mechanisms of the neural circuits, we analyzed the distributional shifts induced by external perturbations (stimuli). While the time-series data in Giovanniello et al. [5] (e.g., Extended Fig. 6o) indicate that the average fluorescence signal typically returns to baseline levels after a stimulus, we hypothesized that the underlying stochastic state of the network might undergo a lasting reconfiguration. To test this, we reconstructed the probability density functions (PDFs) of the neural signals for the time windows immediately before (p_{pre}) and after (p_{post}) the perturbation using Gaussian Kernel Density Estimation (KDE), implemented using the gaussian_kde function from the SciPy library. We then employed the Kullback-Leibler (KL) Divergence to quantify the informational distance between these two temporal states [14]:

$$D_{KL}(p_{\text{post}}||p_{\text{pre}}) = \int_{-\infty}^{\infty} p_{\text{post}}(x) \ln \left(\frac{p_{\text{post}}(x)}{p_{\text{pre}}(x)} \right) dx \tag{1}$$

Here, x represents the neural signal intensity. A non-zero D_{KL} value–even when the mean signal amplitude ($\mathbb{E}[x]$) has returned to baseline–indicates a "distributional hysteresis" (or hidden state shift). This metric reflects the energy cost or plasticity involved in the system's response, revealing that the neural circuit does not simply "reset" but evolves to a statistically distinct state following environmental interaction. We computed the KL Divergence using the kl_div function from the SciPy library's special module, providing a robust way to measure the change in distribution between the pre- and post-perturbation states. (Detailed formulation is provided in Supplementary Materials Section A.3).

2.2.2 Dynamical Perspective

Single Variable Dynamical Model

To characterize the intrinsic stability and temporal evolution of the neural signals, we modeled the BLA-DMS and CeA-DMS pathways as dynamical systems. We focused on the recovery phase post-perturbation, assuming the system follows a trajectory returning to a steady state (approximated as a damped system).

We constructed a phase space defined by two state variables: the signal amplitude x (Z-scored $\Delta f/F$) and its first derivative $\dot{x}$ (rate of change). This formulation captures the system's instantaneous state and its tendency for change. For each experimental condition (Control vs. Stress), we aggregated the observational data to fit a linear dynamical model using Ridge Regression, which is commonly used for regularization and preventing overfitting in linear models. The Ridge Regression model was implemented using the Ridge class from the scikit-learn library (sklearn.linear_model). This single-variable model serves as a baseline to quantify the autogenous stability of each pathway in isolation. (See Supplementary Materials Section. A.5 for details).

Latent Coupling and Interaction Modeling

A critical hypothesis of this study is that environmental stress reshapes the functional coupling between the BLA-DMS and CeA-DMS pathways. However, the available dataset comprises non-simultaneous recordings from different subjects, precluding standard causality analyses (e.g., Transfer Entropy) that require synchronized time-series.

To overcome this, we propose a Latent Dynamical Coupling Model. This model rests on the assumption that while individual instantiations (mice) differ, the underlying dynamical rules governing circuit interactions remain invariant under identical experimental conditions. Therefore, we can reconstruct the "average" interaction rules by extending the phase space to four dimensions: $\{x, \dot{x}, y, \dot{y}\}$, where x and y represent the signals and their first deviatives of the BLA-DMS and CeA-DMS pathways, respectively. We employed a multivariate Ridge Regression to model the system's evolution, decomposing the dynamics of one pathway (let us take x, $\dot{x}$ as an example) into two components:

Intrinsic Dynamics: Driven by its own state $(x, \dot{x})$.

Cross-Pathway Coupling: Driven by the state of the other pathway $(y, \dot{y})$, representing nonlinear interactions.

Crucially, the objective of this coupling model is explanatory rather than predictive. By comparing the regression coefficients–specifically the cross-terms–between Control and Stress conditions, we can quantify how stress modulates the rules of interaction (e.g., inhibition or excitation strength) between these dual pathways, independent of temporal synchronization. (Mathematical formulation provided in Supplementary Materials Section A.6).

2.3 Neural Network Architecture and Design Philosophy

Building on the statistical and dynamical constraints identified in Section 2.2, we propose a Unified Coupled System (UCS) to investigate the computational mechanisms underlying the stress-induced remodeling of amygdala-striatal circuits. Rather than aiming for a biologically exhaustive simulation, we construct a minimalist computational framework focused on a specific mechanism: the pathological shift from goal-directed flexibility to habitual rigidity.

The core of the UCS consists of two coupled Long Short-Term Memory (LSTM) units, chosen for their ability to capture the temporal hysteresis and memory effects observed in our dynamical analysis. Crucially, to emulate the functional divergence between the BLA-DMS and CeA-DMS pathways, we enforce a structural asymmetry between the two units:

The Exploration Unit (x, mimicking BLA-DMS): Designed with low capacity but high sensitivity to error. It is responsible for precision tracking and local exploration (learning), making it functionally dominant in stable environments but vulnerable to noise.

The Control Unit (y, mimicking CeA-DMS): Designed with high capacity and high damping. It serves as a robustness regulator, responsible for maintaining global stability and absorbing perturbations when the x-unit is overloaded.

The interaction between these units is governed by asymmetric error transmission, ensuring a dynamic handover mechanism where the robustness unit (y) engages primarily when the precision unit (x) exceeds its capacity limit.

The external environment is modeled as a time-series signal superimposed with stochastic perturbations. "Stress" is operationally defined not merely as a strong stimulus, but as a regime of high-frequency, high-amplitude perturbations. This setup allows us to test whether the asymmetric coupling rules–specifically, the handover of control from x to y under high load–can spontaneously emerge from the system's adaptation to these statistical environmental changes.

Schematic construction of the neural network is shown in Figure 1. Further details can be found in the supplementary materials, Section A.9.

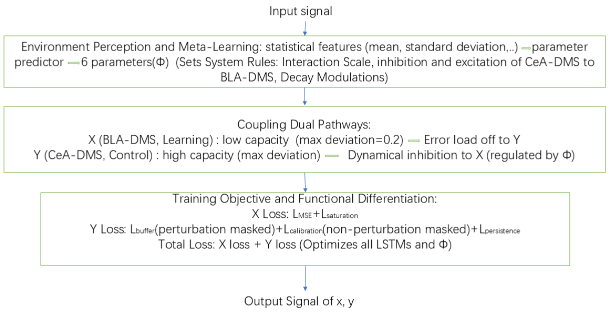
Input signal
Environment Perception and Meta-Learning: statistical features (mean, standard deviation,..) ⟹ parameter predictor ⟹ 6 parameters(Φ) (Sets System Rules: Interaction Scale, inhibition and excitation of CeA-DMS to BLA-DMS, Decay Modulations)
Coupling Dual Pathways:
X (BLA-DMS, Learning) : low capacity (max deviation=0.2) ⟹ Error load off to Y
Y (CeA-DMS, Control) : high capacity (max deviation) ⟹ Dynamical inhibition to X (regulated by Φ)
Training Objective and Functional Differentiation:
X Loss: $L_{MSE}+L_{saturation}$
Y Loss: L_{buffer}(perturbation masked)+$L_{calibration}$(non-perturbation masked)+$L_{persistence}$
Total Loss: X loss + Y loss (Optimizes all LSTMs and Φ)
Output Signal of x, y

Figure 1: Schematic diagram of the meta-learning driven coupled LSTM neural system architecture. The model consists of three layers: the macro-perception layer, the dual-path coupling layer, and the optimization target layer. The core mechanism of the system is meta-learning, which enables adaptive response to the environment and functional differentiation of the pathways through dynamic parameter adjustment.

in Figure 1, there is target asymmetry (Functional Division). This is a design where the BLA-DMS and CeA-DMS units are optimized for different functional objectives, thereby formalizing the functional division between the precision-focused BLA and the stability-focused CeA.

To confirm the stability and generalizability of the learned parameters and functional metrics, we performed a statistical robustness analysis across different model initializations. The final training protocol was repeated using 10 independent random seeds (specifically, seeds $0, 10, 20, \ldots, 90$) for both the Control and Stress conditions. The results of these independent runs were analyzed to calculate the mean, standard deviation, and coefficient of variation for all learned parameters and functional outputs (e.g., Recovery Time and Max Deviation).

3 Results

3.1 Data Analysis

3.1.1 Non-Contingent Stimuli: Aversive Stressor

We first examined the distributional trajectory of neural signals following the acute footshock perturbation. The time-resolved KL divergence (Figure 2) reveals a disparity in the recovery capabilities of the two pathways under stress. In the Control group (blue and green lines), both BLA-DMS and CeA-DMS pathways exhibit a characteristic "perturbation-recovery" pattern: an initial rise in KL divergence followed by a steady decay, indicating that the neural state successfully realigns with its baseline distribution within approximately 4 seconds. However, the Stress group displays a pathological divergence specifically in the BLA-DMS pathway (orange line). Rather than recovering, the KL divergence for Stress BLA-DMS continues to rise dramatically, plateauing at a high level (> 1800) without returning to baseline. Consequently, the Stress group exhibits a significantly larger Integrated KL Divergence (Area Under Curve) in the BLA-DMS pathway compared to Controls (Table 1). In contrast, the Stress CeA-DMS pathway (red line) maintains a relatively low KL divergence throughout the event. This result provides statistical evidence for pathway-specific impairment: chronic stress appears to compromise the homeostatic capacity of the BLA-DMS circuit, causing it to undergo a lasting state shift (hysteresis) after a shock, while the CeA-DMS circuit remains stable and resilient. This asymmetry paves the way for the CeA-DMS pathway to assume dominance in behavioral control.

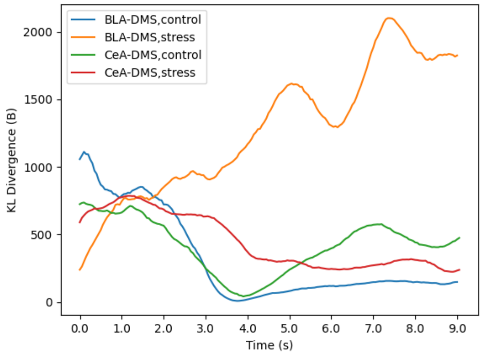

Figure 2: Temporal evolution of KL divergence following footshock.

Table 1: Integrated KL Divergence of Signals of After Footshock Comparing with Corresponding Baselines

Pathway	Control	Stress
BLA-DMS	58288.0087	230198.3955
CeA-DMS	76023.8524	81172.9710

The acute footshock applied to the naive Control group effectively mimics the initial phase of the chronic stress ”training” protocol. By analyzing the phase space stability during this event, we can capture the precise dynamical moment when the neural circuit begins its reconfiguration.The dynamical modeling reveals a stark contrast in stability regimes (Table 2). Crucially, the Control group’s BLA-DMS pathway exhibits a positive eigenvalue ($E_1 = 1.60 \times 10^{-4}$), indicating a mathematically unstable steady state. In the context of our ”Environment-as-Trainer” hypothesis, this instability is not a malfunction but a signature of high plasticity. It suggests that the naive brain, when facing a novel stressor, enters a critical, labile state, essentially, the system is being ”unlocked” to allow for weight updates and circuit reshaping. Conversely, the Stress group exhibits strictly negative eigenvalues (stable attractors) across all pathways. This implies that after 14 days of chronic exposure, the neural networks have converged to a new, rigid equilibrium. The system has ”learned” the stress pattern and locked its parameters to ensure robustness, thereby losing the dynamical flexibility (instability) required for further adaptation. Thus, the transition from Control (Unstable/Plastic) to Stress (Stable/Rigid) maps directly onto the trajectory of a neural network moving from an initial training phase to a converged solution.

Table 2: Eigenvalues derived from Ridge Regression of phase space trajectories post-footshock.

Case	Group	Pathway	Steady State		Eigenvalues		Total Recovery Speed
			x_s	$\dot{x}_s$	E_1	E_2	
FootShock	Control	BLA-DMS	-0.397	0	1.60E-04	-0.27275	0.273
		CeA-DMS	-0.3924	0	-0.4044	-29.469	29.472
	Stress	BLA-DMS	-0.6465	0	-0.837	-27.2812	27.294
		CeA-DMS	-0.1597	0	-0.2615	-26.8716	26.873

The absolute value of the eigenvalue indicates the speed of recovery in each of the directions (Table 2, last column). The total speed can be quantified using the L^2-norm of the eigenvalues (i.e., by calculating the square root of the sum of the squares of the two eigenvalues, similar to how the hypotenuse is calculated in the Pythagorean theorem). The larger the value, the faster the recovery. It can be observed that, apart from the BLA-DMS pathway in the control group following footshock stimuli, the recovery speeds are similar across pathways.

The dynamical model offers a mechanistic explanation for the anomalous KL divergence results. The Control BLA-DMS's positive eigenvalue suggests a "labile" state that actively adjusts its trajectory to seek the baseline (explaining the rapid drop in KL). In contrast, the high KL divergence in Stress BLA (Orange line) combined with its negative eigenvalue suggests that the system has settled into a new, pathological attractor that is topologically distinct from the original baseline. The system is "stable" in the sense that it does not explode to infinity, but it is stably trapped in an aberrant state. Meanwhile, the Stress CeA (Red line) remains effectively regulated, consistent with its role as the rigid, habit-forming controller.

To elucidate the structural mechanism underlying the observed divergence in stability, we employed a multivariate regression approach to quantify the coupling coefficients between the BLA-DMS (x) and CeA-DMS (y) pathways during the footshock event (Table 3 and 4).

Table 3: Coefficients of Inter-region Coupling (Coupling Direction: CeA-DMS to BLA-DMS)

Group	Terms					
	y	$\dot{y}$	xy	$x\dot{y}$	$\dot{x}y$	$\dot{x}\dot{y}$
Control	126.48	2.61	70.67	7.7	19.93	0.67
Stress	7.63	1.62	-24.78	4.5	1.61	1.23

Table 4: Coefficients of Inter-region Coupling (Coupling Direction: BLA-DMS to CeA-DMS)

Group	Terms					
	x	$\dot{x}$	xy	$x\dot{y}$	$\dot{x}y$	$\dot{x}\dot{y}$
Control	90.84	1.59	63.55	34.01	2.8	1
Stress	61.99	-0.01	-46.15	7.8	7.65	0.87

A critical finding is the pervasive sign reversal in the non-linear interaction terms (xy) across both directions. In the Control group, these terms are strongly positive (e.g., $y \to x$, $xy = 70.67$), indicating synergistic communication. However, chronic stress causes these interactions to flip to negative (e.g., $y \to x$, $xy = -24.78$; $x \to y$, $xy = -46.15$), signifying a transition to mutually antagonistic, suppressive coupling. Furthermore, the analysis reveals a directional asymmetry indicative of rigidity:

CeA-DMS → BLA-DMS: The linear influence of CeA-DMS on BLA-DMS (y term) is drastically reduced (from 126.48 to 7.63) in the Stress group. This high coefficient in the Control group suggests that the strong, positive linear coupling from CeA-DMS acts as a high-gain homeostatic force, actively compensating for the inherent instability ($E_1 > 0$) observed in the BLA-DMS dynamics and thus ensuring rapid recovery to baseline (low KL). The drastic reduction of this linear term in the Stress group signifies the loss of this essential high-gain restorative mechanism. Combined with the negative xy term, the CeA-DMS pathway fails to apply the necessary corrective control input, which accounts for the collapse of the BLA-DMS homeostatic mechanism, driving the system towards the pathological state shift observed in Figure 2.

BLA-DMS → CeA-DMS: The coefficient for the BLA-DMS rate of change ($\dot{x}$) on the CeA-DMS pathway drops from a positive value (1.59) in Control to nearly zero (-0.01) in the Stress group. This decoupling from the BLA-DMS's dynamic modulation suggests that the CeA-DMS becomes unresponsive to the exploratory input, reinforcing its rigid and dominant role as a stable, habit-forming controller (consistent with the stable negative eigenvalues observed in Table 2). Collectively, the coupling analysis demonstrates that chronic stress transforms the amygdala-striatal circuit from a balanced, synergistic system into a highly asymmetrical, mutually suppressive network that locks the BLA-DMS into a pathological attractor state. (Detailed coupling model can be found in Supplementary Materials Section A.6)

3.1.2 Contingent Stimuli

Unlike the naive defensive response elicited by footshock, the behaviors analyzed in this section, including bout-initiating presses and reward collection occur within a learned instrumental context. Even though the "unpredicted rewards" were delivered non-contingently, they were presented to mice that had already established strong associations between lever-pressing and food delivery through prior training. Thus, these neural dynamics reflect the operation of a "trained" network executing goal-directed or habitual routines.

As reported by Giovanniello et al. [5], chronic stress did not catastrophically disrupt the mice's ability to perform these basic tasks; the macroscopic behavioral performance remained largely consistent between the Control and Stress groups under standard conditions. However, the underlying neural activity revealed a significant amplitude shift (CeA-DMS' signal strengthened). This discrepancy preserved behavioral competence despite altered neural signaling and suggests a mechanism of functional compensation.

Our analysis of KL divergence across training sessions (from FR-1 to RR-10, see Supplementary Materials Figure A2) exhibits a difference between the two pathways. The CeA-DMS pathway maintains a consistent KL divergence profile across session transitions in both Control and Stress groups. While the KL divergence in BLA-DMS pathway displays some differences across sessions. This suggests that the BLA-DMS pathway serves as an "Exploration Channel" (sensitive to environmental variance), whereas the CeA-DMS pathway functions as a "Stability Channel" (maintaining robust execution regardless of task difficulty).

From a dynamical perspective, the Ridge Regression models for these instrumental tasks consistently yield negative eigenvalues (indicating stable attractors) for both groups (see Supplementary Materials Tables A1 and A6). This implies that the learned instrumental contingency–linking lever pressing to food reward–keeps the neural dynamics of both Control and Stress groups synchronized within a stable operational regime, effectively masking the underlying circuit remodeling during routine tasks.

During unpredicted rewards, the Control group's CeA-DMS pathway exhibits a elevated KL divergence. Crucially, dynamical analysis (Table A1) confirms that this elevation is not a signature of instability (eigenvalues remain negative). Instead, it suggests that in the healthy brain, the CeA-DMS retains adaptive plasticity–actively shifting its state to process the positive salience of the unexpected reward. This implies an efficient functional integration where the BLA-DMS processes reward prediction errors and transmits this information to the CeA-DMS. In contrast, the Stress group lacks this dynamic responsiveness, further confirming its rigid, habit-bound state.

3.2 ANNs Model Simulation

To investigate the mechanism of stress-induced remodeling, we trained independent instances of the Unified Coupled System (UCS) to adapt to distinct environmental statistics. The synthetic input sequences (Figure 3) were designed to capture the statistical characteristics of biological environments:

- Baseline Rhythmicity: A periodic cosine component ($T = 2\pi/80$) simulates predictable environmental cycles (e.g., circadian rhythms, foraging availability).
- Stochastic Uncertainty: Gaussian noise (amplitude 0.3) represents background internal fluctuations.
- Acute Perturbation: A discrete anomalous pulse (amplitude 1.5, index 200) serves as the computational analog of the footshock, probing the system's homeostatic resilience.

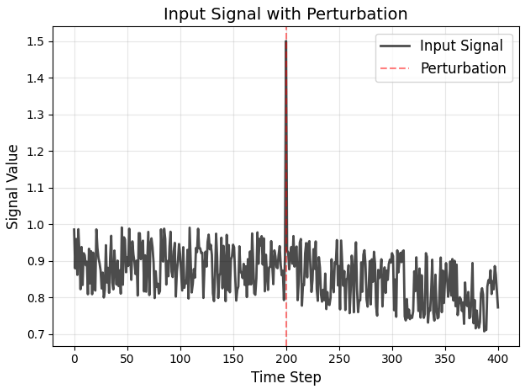

Figure 3: Simulation of test signals. The signal combines predictable periodicity with stochastic noise. The central spike mimics an acute high-impact perturbation (such as footshock), serving as a probe to test circuit stability.

The stable convergence of the total loss function across training epochs (Figure 4) indicates that both models successfully learned their respective environmental statistics, each evolving distinct internal strategies optimized either for precision or stability.

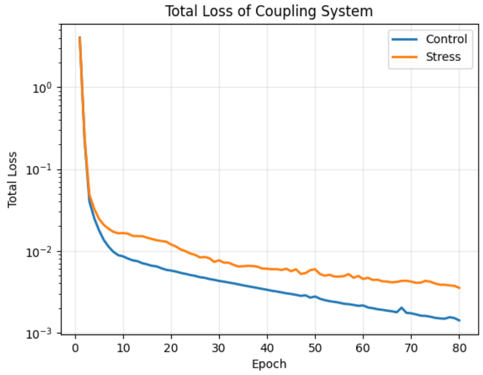

Figure 4: Training Convergence. The stability of the loss function indicates that the UCS successfully learns to predict the environmental statistics.

Based on the initial data analysis, we hypothesized that the BLA-DMS and CeA-DMS pathways serve distinct functional roles: the BLA-DMS pathway is primarily responsible for exploration, while the CeA-DMS pathway is more involved in stability regulation. However, it was only through the neural network simulations that we discovered a critical aspect of this functional asymmetry: in order to accurately replicate experimental results, the computational model necessitated these two pathways be optimized using distinct training objectives (i.e., loss functions). This finding underscores the importance of asymmetry not only in their functional roles but also in their inherent optimization principles during circuit remodeling.

In our simulation, the responses of the two pathways under perturbation were consistent with the experimental observations:

- BLA-DMS Response: In the control group, the BLA-DMS pathway exhibited a strong, transient activation following the perturbation, which quickly returned to baseline (Figure 5(a)). In contrast, the BLA-DMS signal was significantly weaker in the stress group, reflecting the inhibition of BLA-DMS by the CeA-DMS pathway under chronic stress conditions (Figure 5(b)). This finding aligns with the idea that, during chronic stress, CeA-DMS suppresses BLA-DMS activity to reduce exploratory behavior and maintain stability.

- CeA-DMS Response: In contrast, the CeA-DMS pathway exhibited an amplified response in the stress group, showing increased activity following the perturbation (Figure 5(b)). This heightened activity in the stress condition supports the role of CeA-DMS in maintaining stability by self-activating during stress, despite its inhibitory effect on BLA-DMS.

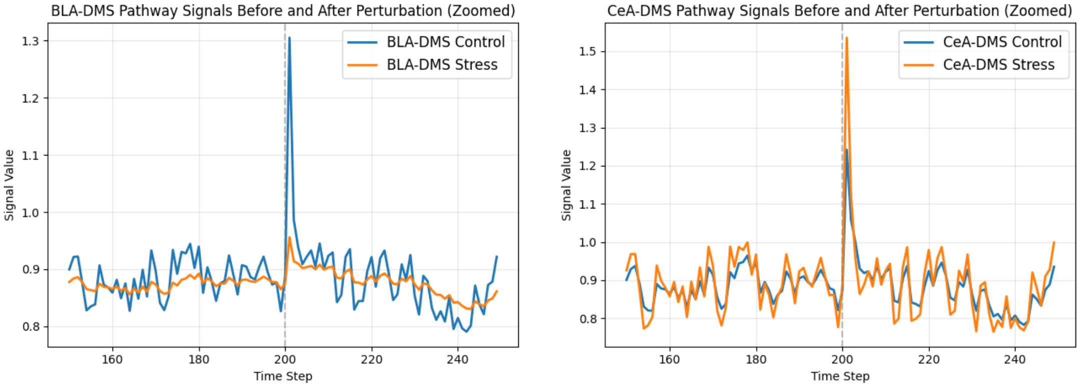

(a) Simulated signals of BLA-DMS pathway

(b) Simulated signals of CeA-DMS pathway

Figure 5: Simulated Pathway Dynamics. The UCS model reproduces the divergent recovery of the BLA-DMS and CeA-DMS pathways under perturbations in control and stress conditions, matching experimental observations.

To ensure the statistical robustness and reproducibility of the learned mechanisms, the model was trained using 10 independent random initial seeds (specifically, seeds $0, 10, 20, \ldots, 90$). The analysis of all learned parameters and functional metrics showed low coefficients of variation (CV), confirming that the solution space is highly stable and the resulting ANN model is robust (Detailed statistics in Supplementary Table A11).

As shown in Figure 6, the Max Deviation of N1 (representing the state of the BLA-DMS pathway) clearly demonstrated the mechanistic divergence. The mean value of the Control group was 0.3389, compared to 0.0570 for the Stress group. This difference is mechanistically linked to the dynamic range of the BLA-DMS component. Specifically, the Max Deviation of BLA-DMS in the Control group (0.339) exceeded the intrinsic capacity (0.2), leading to prolonged saturation and recovery. In contrast, Stress models maintained BLA-DMS within an extremely low range (0.057), indicating a learned strategy of instantaneous suppression of the BLA-DMS component.

The suppression of BLA-DMS in the Stress group was achieved by a high-gain activation of the CeA-DMS component. The Max Deviation of N2 (representing the state of the CeA-DMS pathway) in the Stress condition (0.670) was nearly double that of the Control condition (0.339), demonstrating that Stress models utilize CeA-DMS's high capacity to generate a powerful, transient inhibitory signal to enforce system stability.

Crucially, the functional analysis revealed a robust divergence in system elasticity. The Recovery Time for the Control models (3.00 ± 0.77 steps) was significantly longer (3 times longer) than that for the Stress models (1.00 ± 0.00 steps) (See Figure 6). This quantitative simulation result is consistent with the experimental observation that the Control group exhibits prolonged instability (longer recovery time) following acute perturbation.

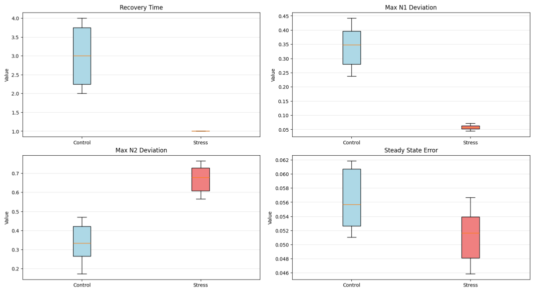

Figure 6: Robustness test for the ANN model. These Figure show the response to perturbation.

4 Conclusion and Discussion

This study aimed to bridge the gap between behavioral and neural responses to chronic stress by leveraging both experimental data analysis and neural network modeling. While previous work has demonstrated behavioral rigidity and neural signal changes in stress-exposed rodents, the underlying mechanisms have remained unclear. By first analyzing existing data and then using a Unified Coupled System (UCS) neural network, we identified key insights into how chronic stress remodels neural circuits and compromises adaptive behaviors.

4.1 Key Insights from Data Analysis

In the initial data analysis, we investigated the distributional trajectory of neural signals in response to an acute footshock perturbation. We observed differences in the recovery dynamics of the BLA-DMS and CeA-DMS pathways either in KL divergence, dynamical stability or coupling:

KL Divergence: In the Control group, both pathways exhibited a typical ”perturbation-recovery” pattern, returning to baseline within a few seconds. In contrast, the BLA-DMS pathway in the Stress group failed to recover and remained in a pathological state, while CeA-DMS activity remained stable and resilient. This indicated that chronic stress selectively impaired the BLA-DMS pathway, locking it into a maladaptive state, while CeA-DMS maintained stability.

Dynamical Stability: In response to the simulated chronic stress perturbations (footshock), eigenvalue analysis confirmed that while the Control group exhibited instability in the BLA-DMS pathway, indicative of high plasticity, the Stress group showed stable, rigid attractors in all pathways, reflecting a loss of the dynamic flexibility necessary for further adaptation. This shift from plasticity to rigidity parallels the convergence of neural circuits observed in the UCS simulations.

Pathway Coupling: Regression analysis of pathway interactions revealed that chronic stress disrupted the synergistic coupling between the BLA-DMS and CeA-DMS pathways. In the Control group, strong positive coupling facilitated adaptive recovery, while in the Stress group, antagonistic coupling emerged, reflecting a rigid, suppressive relationship between the pathways.

Consistent with the findings of Giovanniello et al., our data analysis suggests that chronic stress exposure did not significantly affect the mice’s ability to perform basic tasks. Both the KL divergence analysis and dynamical modeling show that performance in the stress group remained largely unaffected under standard conditions. However, as noted by Giovanniello et al., changes in the environment, such as reward unpredictability, resulted in behavioral alterations. In line with this, our analysis revealed that, in the Control group, the KL divergence of the CeA-DMS pathway increased significantly under these altered conditions, indicating a substantial shift in signal dynamics. In contrast, the Stress group showed relatively stable CeA-DMS signals, suggesting a compensatory mechanism that maintained stability despite environmental perturbations.

4.2 Neural Network Simulations: Validating the Mechanisms

Following the data analysis, we used the Unified Coupled System (UCS) neural network to test the hypothesized functional roles of BLA-DMS and CeA-DMS. The neural network was designed based on the experimental observations, with distinct functional objectives for each pathway: BLA-DMS was optimized for precision (exploration), while CeA-DMS was optimized for stability (homeostasis).

The simulations successfully reproduced the key dynamics observed in the experiment:

BLA-DMS under Stress: In the Stress model, the BLA-DMS pathway exhibited reduced activity following the perturbation, reflecting the suppression of exploratory behavior under chronic stress. This contrasted with the Control model, where BLA-DMS showed a strong signal response. This behavior aligns with the experimental finding that chronic stress inhibits the BLA-DMS pathway, leading to reduced flexibility and exploration.

CeA-DMS under Stress: The CeA-DMS pathway in the Stress model showed increased signal strength, consistent with its role in maintaining stability under stress. This amplification of CeA-DMS activity is aligned with the idea that under stress, the CeA-DMS pathway assumes a dominant, compensatory role to ensure behavioral stability, even at the expense of exploratory flexibility.

The key result from the UCS simulation was the realization that the BLA-DMS and CeA-DMS pathways not only serve different functional roles but also require distinct optimization targets for successful simulation. This was not immediately apparent from the initial data analysis but emerged as a critical finding through the neural network simulations. The BLA-DMS pathway required a precision-focused optimization target to recover rapidly from perturbations, while the CeA-DMS pathway required a stability-focused optimization target to maintain its homeostatic role under chronic stress.

This discovery confirms the functional division between the two pathways, with BLA-DMS supporting exploration and adaptability, and CeA-DMS serving as a rigid, stability-maintaining mechanism. The neural network simulations, by incorporating these asymmetrical training targets, successfully replicated the divergent behavior of the pathways under stress, providing computational validation for the mechanisms observed in vivo.

The robustness of these functional findings was confirmed by performing a stability analysis using 10 independent random initial seeds (see Supplementary Table A11 for detailed statistics). This analysis yielded a reproducible divergence in system elasticity. Crucially, the Recovery Time for the Control models (3.00 ± 0.77 steps) was consistently three times longer than that for the Stress models (1.00 ± 0.00 steps) (Figure 6). This quantitative difference strongly validates the hypothesis that chronic stress enhances the system's ability to achieve stability following acute perturbation.

Mechanistically, the stability analysis revealed that the prolonged recovery in the Control group was caused by the BLA-DMS pathway exceeding its capacity (0.339), while the rapid recovery in the Stress group was achieved through high-gain activation of CeA-DMS (with mean value 0.670) which instantaneously suppressed BLA-DMS (with mean value 0.057).

4.3 Conclusion: Linking Behavioral and Neural Dynamics

In summary, this study integrates data analysis and neural network modeling to elucidate the mechanisms behind stress-induced circuit remodeling. Chronic stress leads to instability within the system, prompting the CeA-DMS pathway to take on a dominant role in maintaining stability. This shift suppresses the exploratory function of the BLA-DMS pathway, ultimately resulting in behavioral rigidity. These findings highlight the trade-off between flexibility and robustness that occurs during chronic stress, offering new insights into how the brain adapts to persistent environmental challenges.

The UCS neural network model revealed that the BLA-DMS and CeA-DMS pathways not only have distinct functional roles but also different built-in optimization goals from the outset. The CeA-DMS pathway's primary optimization goal is stabilization and homeostasis, which is an inherent design feature rather than something learned. In a stable environment, without chronic stress i.e. frequent perturbations, this goal does not come into play, allowing the BLA-DMS pathway to dominate exploration and precision. However, when the system is destabilized under stress, the CeA-DMS pathway's stabilizing function is activated, reflecting the system's built-in design to prioritize stability when needed. This shift, though appearing to result from stress-induced learning, is actually a manifestation of the system's inherent optimization goals, where stabilization takes precedence when the environment demands it.

Furthermore, the analysis of Coefficient of Variation (CV) across the 10 runs provided computational insight into the stability-flexibility trade-off in the two conditions. While the Stress model achieved extreme rigidity in its functional output (Recovery Time with CV=0.00), the Control model retained a higher functional variance (Recovery Time with CV=0.26), suggesting a greater degree of intrinsic functional flexibility in the absence of chronic pressure. This inherent flexibility in the Control group, though crucial for adaptation and exploration, may also be the source of its vulnerability to instability following acute shock. Conversely, the high CV observed in the CeA-DMS $\rightarrow$ BLA-DMS coupling weights (CV ≈ 0.40; Supplementary Table A11) confirms that the system preserves structural flexibility (functional compensation), even under stress, ensuring that the rigid functional output is achieved through a robust, adaptable underlying structure.

A Supplementary Materials

A.1 Supplementary Graphs, Tables and Results

A.1.1 Non-Contingent Stimuli: Footshock and Unpredicted Reward

Single Variable Dynamical Model

After constructing the models post-perturbation using ridge regression, the stability of the model's orbits near the steady states (represented by x_s and $\dot{x}_s$, the subscript s denotes "steady state") is analyzed and presented in Table A1. Detailed models can be consulted in supplementary materials section A.5 Table A14. The stability is determined by the eigenvalues (E_1 and E_2) of the Jacobian matrix, which correspond to the two dimensions of the phase space. When both eigenvalues are negative, the orbits converge towards the steady state. However, if either of the eigenvalues becomes positive, the orbits will diverge, indicating that the system loses stability.

Table A1: Steady State Values, Eigenvalues and Total Recovery Speed for Each Group and Pathway

Case	Group	Pathway	Steady State		Eigenvalues		Total Recovery Speed
			x_s	$\dot{x}_s$	E_1	E_2	
FootShock	Control	BLA-DMS	-0.397	0	1.60E-04	-0.27275	0.273
		CeA-DMS	-0.3924	0	-0.4044	-29.469	29.472
	Stress	BLA-DMS	-0.6465	0	-0.837	-27.2812	27.294
		CeA-DMS	-0.1597	0	-0.2615	-26.8716	26.873
Unpredicted Reward	Control	BLA-DMS	0.0331	0	-1.5011	-27.7207	27.761
		CeA-DMS	-0.1326	0	-1.7699	-27.7119	27.768
	Stress	BLA-DMS	-0.3153	0	-1.7012	-27.2792	27.332
		CeA-DMS	0.5462	0	-1.0187	-25.9814	26.001

In Table A1, it is evident that the steady state of the control group, which is rarely stimulated by footshock, may lose stability in the BLA-DMS pathway. The eigenvalue is very close to zero, and considering the errors inherent in the regression-based model, this point can be regarded as a critical threshold. If this were a theoretical model based solely on differential equations, this steady state would undoubtedly be unstable.

In Table A1, we observe that the difference between the steady states of the two pathways is smaller in the control group compared to the stress group. For footshock stimuli, the steady state in the BLA-DMS pathway in the stress group is stable at -0.6465, showing a clear deviation from the control group's steady state of -0.397. This suggests that after 14 days of chronic stress exposure, the steady state of the BLA-DMS pathway has shifted. Given the complexity of the system, this may indicate that it has undergone a non-equilibrium phase transition.

The absolute value of the eigenvalue indicates the speed of recovery in each of the directions. The total speed can be quantified using the L^2-norm of the eigenvalues (i.e., by calculating the square root of the sum of the squares of the two eigenvalues, similar to how the hypotenuse is calculated in the Pythagorean theorem). The larger the value, the faster the recovery. It can be observed that, apart from the BLA-DMS pathway in the control group following footshock stimuli, the recovery speeds are similar across pathways.

KL Divergence

The brain constantly processes information, with external perturbations introducing additional informational load. KL divergence between pre- and post-perturbation distributions reflects this change, indicating how much more information the brain needs to process in response to a given stimulus.

Figure A1 depicts temporal evolution of KL divergence following unpredicted reward, computed by comparing the distribution of neural activity within a sliding time window to the baseline distribution prior to the perturbation, across different pathways and experimental groups.

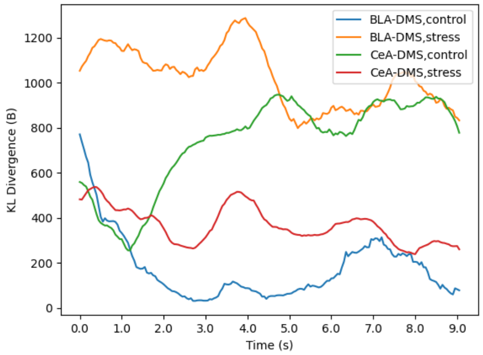

Figure A1: BLA-DMS and CeA-DMS response to unpredicted reward

As shown in Table A2, the steady-state signal level after the perturbation is lower than the baseline mean, suggesting that neural activity is suppressed in both pathways.

The integrated KL divergences in both pathways of the control group are within a similar range. In the stress group, the CeA-DMS pathway also shows an integrated KL divergence at a comparable level. However, the BLA-DMS pathway in the stress group exhibits a markedly higher integrated KL divergence, indicating a substantial increase in information processing demand in this pathway under stress. Specifically, the BLA-DMS pathway in the stress group shows an integrated KL divergence of 230,198.3955, nearly four times that of the control group (58,288.0087). Detailed values are provided in Table A3.

Table A2: Mean and Standard Deviation Change for Each Group and Pathway

Case	Group	Pathway	Baseline Mean (Pre)	Baseline Mean (Post)	ΔMean (Post-Pre)	ΔStd(Post-Pre)
FootShock	Control	BLA-DMS	0.0252	-0.397	-0.4222	0.0832
		CeA-DMS	0.2392	-0.3924	-0.6316	0.1804
	Stress	BLA-DMS	0.2294	-0.6465	-0.8759	0.0884
		CeA-DMS	0.1392	-0.1597	-0.2989	0.2692
Unpredicted Reward	Control	BLA-DMS	0.0474	0.0331	-0.0143	0.1324
		CeA-DMS	0.0849	-0.1326	-0.2175	0.3418
	Stress	BLA-DMS	0.1182	-0.3153	-0.4335	0.2384
		CeA-DMS	-0.1213	0.5462	0.6675	0.0541

For the unpredicted reward condition, the evolution of KL divergence in the BLA-DMS pathway of the control group resembles that in the CeA-DMS pathway of the stress group. In contrast, the KL divergence trajectory in the CeA-DMS pathway of the control group and the BLA-DMS pathway of the stress group become similar starting approximately 4 seconds after the perturbation.

As shown in Table A2, following the perturbation, signal means decreased across all conditions except for the CeA-DMS pathway in the stress group, where a marked increase was observed. This suggests that neural activity was generally suppressed by the perturbation, with the exception of this particular pathway under stress.

Additionally, the standard deviations increased in all conditions except for the CeA-DMS pathway in the stress group, where a reduction was observed. The overall increase in variability indicates that perturbations not only modulate signal magnitude but may also induce a reorganization of neural activity patterns.

Table A3: Integrated KL Divergence of Signals of After Stimuli Comparing with Corresponding Baselines

	Control		Stress	
Pathway	FootShock	Unpredicted Reward	FootShock	Unpredicted Reward
BLA-DMS	58288.0087	32014.9568	230198.3955	186145.2347
CeA-DMS	76023.8524	133727.7601	81172.9710	66962.0120

Following an unexpected, unpleasant stimulus, the brains of control mice entered a metastable state. This response, characterized by a slow recovery speed (0.273 for the BLA-DMS pathway), represents an efficient and adaptive strategy for learning and exploration, as it allows the system to process information without incurring significant energy costs. This process can be interpreted as the brain maintaining a dynamic, flexible state to facilitate the encoding of new environmental cues. In contrast, mice exposed to chronic stress exhibited a different response. Their brains, when faced with the same stimulus, rapidly transitioned to a stable steady state, with a significantly faster recovery speed (27.294 for the BLA-DMS pathway). This rapid shift, however, came at the expense of a substantial increase in information processing cost, as measured by the KL divergence.

We propose that if the control group were exposed to chronic stress for a long time, their brain's dynamic state would be reshaped, sacrificing the time-intensive process of exploration in favor of a rapid but energetically expensive transition to a defensive stable state.

However, the unpredicted reward, being a pleasant stimulus, does not drive the brain's pathways into a metastable state. In the control group, the response in the BLA-DMS pathway is similar to that seen after footshock, while the CeA-DMS pathway shows a more significant change in state. This suggests that the brain is evaluating whether the reward might pose a potential threat.

In contrast, in the stress group, the state of the BLA-DMS pathway changes similarly to that observed after footshock, indicating that prolonged exposure to chronic stress may lead the brain to rapidly stabilize the system, without considering the energy cost of this process. However, the CeA-DMS pathway shows only a modest change, and the signal strength of the new steady state is larger than the pre-perturbation steady state. This suggests that, although the brain system reaches stability and appears normal, it has been reshaped to respond to external stimuli.

The inferences are drawn from our dynamical and statistical analyses. Additionally, the coupling model will serve as further evidence to support these inferences.

Coupling Model

Tables A4 and A5 show the coefficients of inter-region coupling terms. We focus on the terms with large coefficients, as they make the most significant contributions to the overall coupling dynamics.

In the footshock case, the coupling from CeA-DMS to BLA-DMS in the control group shows large coefficients for both the linear term (y) and the nonlinear term (xy), confirming that the perturbation destabilizes the BLA-DMS pathway (Table A4, row 1). At the same time, CeA-DMS exerts a strong corrective influence, as reflected by the large coupling coefficients, demonstrating that CeA-DMS is actively adjusting the system. In contrast, in the stress group, the linear coefficient (y) is smaller, and the nonlinear coefficient (xy) becomes negative (Table A4, row 2). This suggests that CeA-DMS exerts a suppressive influence, driving the BLA-DMS pathway toward a stable steady state.

For the coupling from BLA-DMS to CeA-DMS in the control group, both the linear coefficient (x) and the nonlinear term (xy) are relatively large. Since the CeA-DMS pathway remains stable, the coefficient for x is not as large as y, but both coefficients are positive, indicating that the two pathways are working synergistically (Table A5, row 1). In the stress group, the nonlinear term (xy) becomes negative, suggesting that BLA-DMS is also suppressing the information transmission from CeA-DMS. However, the coefficient for x remains positive and relatively large, indicating that BLA-DMS was initially poised to explore the new stimulus, but this exploration was blocked by CeA-DMS (Table A5, row 2). The consequence of this blockade is reflected in a significant increase in KL divergence following the perturbation in this pathway (Table A3).

Table A4: Coefficients of Inter-region Coupling (Coupling Direction: CeA-DMS to BLA-DMS)

Case	Group	Terms					
		y	$\dot{y}$	xy	$x\dot{y}$	$\dot{x}y$	$\dot{x}\dot{y}$
FootShock	Control	126.48	2.61	70.67	7.7	19.93	0.67
	Stress	7.63	1.62	-24.78	4.5	1.61	1.23
Unpredicted Reward	Control	75.2	2.34	83.57	-0.81	-16.29	0.85
	Stress	-22.14	5.11	-30.7	14.95	-14.55	-1.06

Table A5: Coefficients of Inter-region Coupling (Coupling Direction: BLA-DMS to CeA-DMS)

Case	Group	Terms					
		x	$\dot{x}$	xy	$x\dot{y}$	$\dot{x}y$	$\dot{x}\dot{y}$
FootShock	Control	90.84	1.59	63.55	34.01	2.8	1
	Stress	61.99	-0.01	-46.15	7.8	7.65	0.87
Unpredicted Reward	Control	48.17	0.32	5.76	-0.49	-5.56	0.35
	Stress	17.93	0.71	2.54	-7.11	0.74	-1.67

In the unpredicted reward case, the coupling from CeA-DMS to BLA-DMS in the control group is characterized by relatively large coefficients for both the linear term (y) and the nonlinear term (xy), although these are smaller than in the footshock condition (Table A4, row 3). From single variable model (Table A1), we know that the BLA-DMS pathway in the control group does not destabilize after this perturbation, indicating that CeA-DMS continues to perform its "alert" and "evaluation" functions. An unpredicted reward is itself a signal that requires evaluation. CeA-DMS ensures that BLA-DMS can process this information stably, but because the reward is not perceived as a threat, the regulatory influence is weaker compared to the footshock case.

For the coupling from BLA-DMS to CeA-DMS, the influence is primarily reflected in the linear term (x), and the interaction is cooperative (Table A5, row 3). This suggests that BLA-DMS focuses on its core function of efficiently processing reward information and passing the results to CeA-DMS for integration. The system remains stable without destabilization. This indicates that the two pathways handle rewards through cooperative interactions to ensure learning and adaptation.

In the stress group, the coupling from CeA-DMS to BLA-DMS shows large negative coefficients for both y and xy, indicating that CeA-DMS adopts a suppressive strategy, perceiving the unpredicted reward as a potential threat that needs to be shut down. The nonlinear terms ($x\dot{y}$ and $\dot{x}y$) have similar absolute values but opposite signs, reflecting dynamic and contradictory interactions between the two pathways (Table A4, row 4). The signal strength of CeA-DMS (y) attempts to slow down the rate of change in BLA-DMS ($\dot{x}$), while the rate of change in CeA-DMS ($\dot{y}$) drives the change in BLA-DMS (x). This indicates an internal conflict between the two pathways, where CeA-DMS attempts to suppress BLA-DMS but cannot fully do so, leading to a state of "suppression but not complete inhibition." For the coupling from BLA-DMS to CeA-DMS, BLA-DMS still exerts a positive influence on CeA-DMS (linear term x), but this influence is not coordinated with the suppressive behavior of CeA-DMS. This further confirms the collapse of the cooperative relationship between the two pathways (Table A5, row 4).

A.1.2 Contingent Instrumental Behaviors

Steady States of Single Variable Models

The mice were trained to press a lever to gain food under different reinforcement schedules: a fixed ratio (FR-1) with a 100% reward probability, and random ratios (RR-2, RR-5, RR-10), with an average of 2, 5, and 10 lever presses per reward, respectively. This setup results in a decreasing probability of receiving food after each lever press. The lever-pressing behavior and the associated food reward stimuli are fully anticipated by the mice.

In a manner similar to the single-variable model for unexpected stimuli in section A.1.1, the post-perturbation models were constructed using ridge regression to analyze the stability of the model's orbits near the steady states. The results are presented in Table A6. As the steady state of $\dot{x}_s \equiv 0$, this steady state is not explicitly presented in Table A6.

Table A6: Steady State Values, Eigenvalues and Total Recovery Speed for Each Group, Pathway and Sessions

			Bout-Initiating Presses				Reward			
Group	Pathway	Session	Steady State	Eigenvalues		Total Recovery Speed	Steady State	Eigenvalues		Total Recovery Speed
			x_s	E_1	E_2		x_s	E_1	E_2	
Control	BLA-DMS	FR-1	0.0276	-0.689	-23.148	23.158	0.0013	-0.381	-27.708	27.711
		RR-2	0.1811	-0.928	-26.292	26.308	0.0177	-0.693	-25.399	25.408
		RR-5	0.0239	-0.594	-25.266	25.273	-0.0006	-0.66	-26.6	26.608
		RR-10	-0.0599	-0.788	-25.429	25.441	0.0033	-0.861	-26.687	26.701
	CeA-DMS	FR-1	-0.2178	-1.724	-26.294	26.350	-0.1512	-0.713	-28.548	28.557
		RR-2	-0.2642	-1.11	-27.113	27.136	-0.0913	-0.618	-26.303	26.310
		RR-5	-0.1903	-0.576	-29.081	29.087	0.0034	-0.279	-28.842	28.843
		RR-10	-0.1484	-0.775	-28.687	28.697	-0.0149	-0.56	-29.316	29.321
Stress	BLA-DMS	FR-1	-0.4853	-0.36	-28.181	28.183	-0.5228	-0.603	-24.869	24.876
		RR-2	-0.5101	-0.417	-27.402	27.405	-0.4532	-0.594	-27.145	27.151
		RR-5	-0.4142	-1.033	-27.42	27.439	-0.3854	-0.721	-25.985	25.995
		RR-10	-0.3598	-0.69	-27.186	27.195	-0.3761	-0.766	-24.669	24.681
	CeA-DMS	FR-1	-0.0084	-0.559	-28.189	28.195	0.0746	-0.536	-27.787	27.792
		RR-2	0.0244	-0.353	-28.036	28.038	0.1005	-0.651	-27.615	27.623
		RR-5	0.1262	-0.869	-26.4	26.414	0.2809	-0.512	-28.89	28.895
		RR-10	0.1567	-0.69	-27.569	27.578	0.3647	-1.493	-25.511	25.555

All post-perturbation model trajectories converge to their steady states with similar recovery speeds. This suggests that, regardless of whether the press-initiating signals or the reward signals following the press are based on anticipatory cues, the evolution of the signals remains stable.

KL Divergence of Each Sessions

KL divergence between pre- and post-perturbation distributions reflects the additional informational load change, indicating how much more information the brain needs to process in response to bout-initiating pressing or reward. Table A7 gives the integrated KL divergence of signals after pressing or reward comparing with corresponding baselines. The evolution of integrated KL divergence across sessions is shown in Figure A2. For the BLA-DMS pathway, the integrated KL divergence of bout-initiating pressing and following reward differs between the control and stress groups as the probability of obtaining a reward decreases. For instance, in FR-1, the stress group is with higher values compared to the control group. In contrast, the evolutions in the CeA-DMS pathway are similar across groups, though the absolute values are different.

Taking Table A8 into consideration, it is observed that in the BLA-DMS pathway, the baseline values before the bout-initiating pressing and reward (i.e., pre-action baseline) in the control group are either larger than or approximately equivalent to the values after the action stabilizes (i.e., post-action baseline). In the stress group, however, the post-action baseline values for both bout-initiating pressing and reward are lower than the pre-action baseline. This may result from the suppressive influence of the CeA-DMS

Table A7: Integrated KL Divergence of Signals of After Pressing or Reward Comparing with Corresponding Baselines

		Control		Stress	
		Bout-Intiating Press	Reward	Bout-Intiating Press	Reward
BLA-DMS	FR-1	24628.3111	67363.0906	138602.285	165446.9525
	RR-2	59740.1261	164692.6374	54328.1735	106988.067
	RR-5	58880.9597	47952.8292	50431.407	51027.0478
	RR-10	22790.2484	150934.1416	175500.3375	111623.2633
CeA-DMS	FR-1	6971.1867	28829.5106	6986.8442	25437.3199
	RR-2	49637.9247	7813.3596	44550.334	88744.878
	RR-5	113842.1069	59462.2021	80287.7987	228442.7475
	RR-10	18125.9975	71724.0453	53093.0952	186212.5902

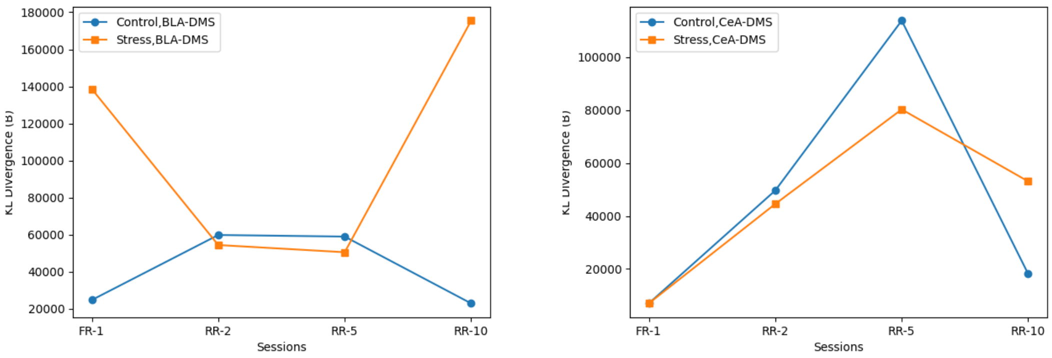

(a) BLA-DMS pathway, bout-initiating pressing (b) CeA-DMS pathway, bout-initiating pressing

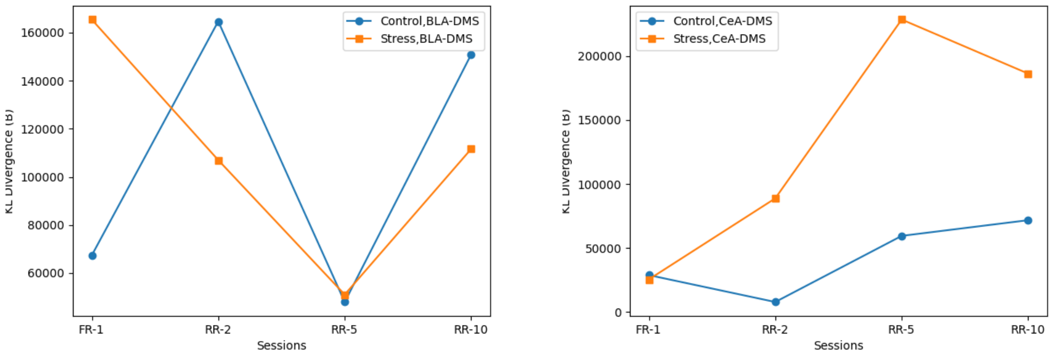

(c) BLA-DMS pathway, reward (d) CeA-DMS pathway, reward

Figure A2: Integrated KL divergence in BLA-DMS and CeA-DMS pathways after bout-initiating press or reward

pathway.

In the CeA-DMS pathway, for the control group, the pre-action baseline for bout-initiating pressing is larger than the post-action baseline, while for reward, the post-action baseline is larger than the pre-action baseline. In contrast, in the stress group, the post-action baseline for bout-initiating pressing is either

Table A8: Mean and Standard Deviation Before and After Perturbation for Each Group, Pathway and Sessions

			Bout-Initiating Presses				Reward			
Group	Pathway	Session	Baseline Mean (Pre)	Baseline Mean (Post)	ΔMean (Post-Pre)	Δ Std(Post - Pre)	Baseline Mean (Pre)	Baseline Mean (Post)	ΔMean (Post - Pre)	Δ Std(Post - Pre)
Control	BLA-DMS	FR-1	-0.1646	0.0276	0.1922	0.0869	-0.1148	0.0013	0.1161	0.1877
		RR-2	0.0396	0.1811	0.1415	0.2244	0.0612	0.0177	-0.0435	0.2611
		RR-5	-0.0949	0.0239	0.1188	0.1003	-0.1299	-0.0006	0.1293	0.1454
		RR-10	-0.0327	-0.0599	-0.0272	0.0665	-0.1798	0.0033	0.1831	0.171
	CeA-DMS	FR-1	-0.1787	-0.2178	-0.0391	0.0505	-0.1696	-0.1512	0.0184	0.149
		RR-2	-0.0686	-0.2642	-0.1956	0.1011	-0.1929	-0.0913	0.1016	0.0354
		RR-5	-0.0531	-0.1903	-0.1372	0.1216	-0.0859	0.0034	0.0893	0.1201
		RR-10	-0.0401	-0.1484	-0.1083	0.0908	-0.174	-0.0149	0.1591	0.2173
Stress	BLA-DMS	FR-1	-0.0477	-0.4853	-0.4376	-0.0182	-0.1056	-0.5228	-0.4172	0.1396
		RR-2	-0.0977	-0.5101	-0.4124	0.0056	-0.1962	-0.4532	-0.257	0.0319
		RR-5	-0.1946	-0.4142	-0.2196	0.1625	-0.2327	-0.3854	-0.1527	0.1476
		RR-10	-0.0601	-0.3598	-0.2997	0.1978	-0.1126	-0.3761	-0.2635	0.1737
	CeA-DMS	FR-1	-0.079	-0.0084	0.0706	0.0064	-0.0623	0.0746	0.1369	-0.0506
		RR-2	-0.1014	0.0244	0.1258	0.1256	-0.2146	0.1005	0.3151	0.1534
		RR-5	-0.1004	0.1262	0.2266	0.0689	-0.1458	0.2809	0.4267	0.171
		RR-10	-0.0586	0.1567	0.2153	0.1029	-0.0959	0.3647	0.4606	0.0707

larger than or approximately equivalent to the pre-action baseline, and the post-action baseline for reward is also larger than the pre-action baseline.

Additionally, it is found that in the CeA-DMS pathway, the greater the uncertainty for reward, the larger the difference between the post-action and pre-action baselines.

These findings suggest that the BLA-DMS pathway serves as the exploratory channel, while the CeA-DMS pathway functions as the stability channel. Although the stress group's brain can be considered a pre-trained neural network–meaning the "weight parameters" differ from those of the control group–the function of the CeA-DMS pathway remains unchanged. The observed changes primarily stem from the BLA-DMS pathway.

The temporal evolution of KL divergence following bout-initiating pressing and reward across sessions is shown in Figures A3 and A4. Although the integrated KL divergence data shown in Figures 2(b) and 2(d) suggest that the behavior of the CeA-DMS pathway is similar between both groups, closer examination of the temporal evolution reveals differences. In the control group, the temporal evolution of both pathways is generally similar, with any phase differences being relatively small, except for the reward in the RR-2 session (see Figure 4(b)). In the stress group, the temporal evolution of both pathways only becomes similar when the uncertainty is large, such as in the RR-10 session (see Figures 3(d) and 4(d)). This suggests that under conditions of high uncertainty, the evolution of both pathways converges, while under lower uncertainty, there is a greater phase difference in their temporal evolution.

This suggests that in the control group, the two pathways are cooperating, while in the stress group, the two pathways may be in conflict. Under high uncertainty, the control group utilizes a flexible strategy to cope with the uncertainty, whereas the stress group relies on a high-energy cost strategy, using brute force to deal with the uncertainty, even though their behavioral outcomes appear similar (Giovanniello et al., 2025 [5]).

Coupling Model For Each Sessions

The coupling direction from CeA-DMS to BLA-DMS (Table A9) shows that the sign of the coefficient for y is consistent between the control and stress groups (Table A9, column 3). This suggests that the motivational drive for lever-press behavior in both groups is similar. However, there were differences in the modulation of dynamic terms (i.e. $x\dot{y}$, $\dot{x}y$) between the groups, indicating that the mechanisms regulating the coupling are distinct under different conditions.

After reward delivery, the coefficient of y in the control group is generally small in magnitude and mostly negative, suggesting that the control group does not exhibit a strong excitatory response to predicted rewards(Table A9, column 9). In contrast, the stress group showed more positive values for y, indicating that rewards elicited a greater excitatory response in this group. Only under the RR-10 session does the

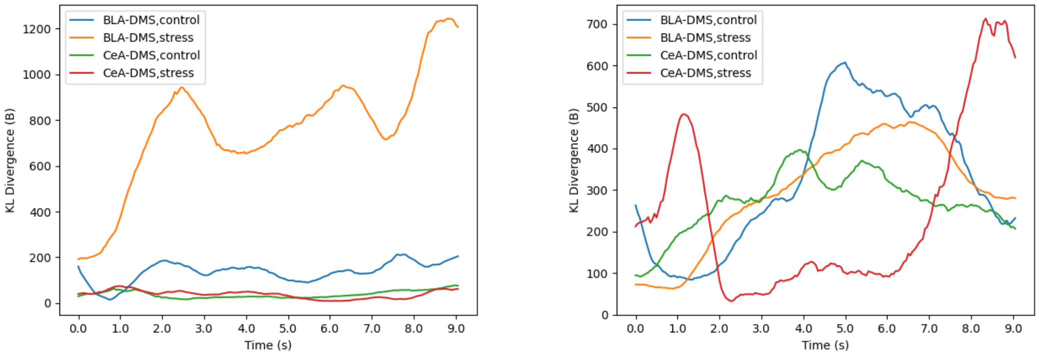

(a) FR-1 (b) RR-2

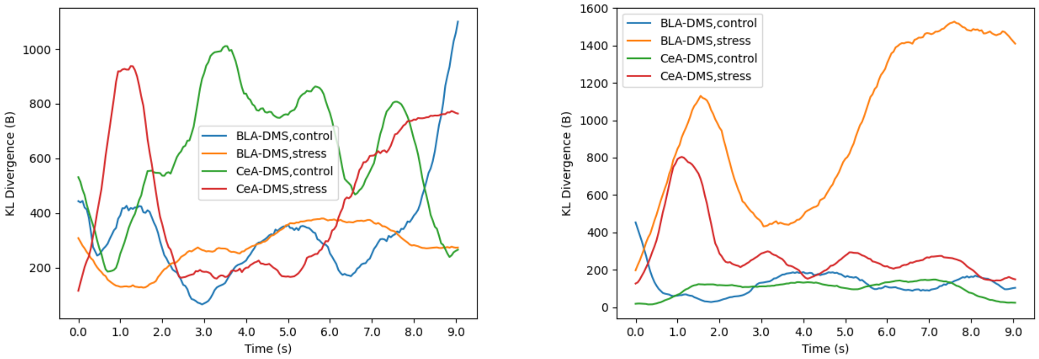

(c) RR-5 (d) RR-10

Figure A3: BLA-DMS and CeA-DMS KL divergence after bout-initiating press

coefficient become small, indicating that high uncertainty reduced the excitatory response in the stress group. This suggests that while expected rewards do not significantly excite the control group, they may induce excitement in the stress group, with this response becoming inhibitory under high uncertainty.

When rewards were delivered, the coefficients for the dynamic terms (xy) are the same for both groups (Table A9, column 11). In the case of a certain reward (FR-1), the coefficients were positive, indicating that the CeA-DMS to BLA-DMS pathway has a facilitatory effect on behavior. However, when the reward is uncertain, the coefficients became negative for both groups, suggesting that the CeA-DMS pathway exerted an inhibitory influence on the BLA-DMS, particularly under conditions of reward uncertainty.

Regarding lever-press behavior, the coefficients for xy are positive in the control group (Table A9, column 5), indicating that lever pressing is driven by motivational factors. In the stress group, however, as the level of uncertainty increased (e.g., under RR-5 and RR-10 conditions), the coefficients for xy become negative, suggesting that increasing uncertainty shifts the motivational response from facilitation to inhibition. This may reflect a more conservative behavioral strategy under stress, where the CeA-DMS's role in modulating motivation transitions from promoting to suppressing the lever-press action in the face of increased uncertainty.

Coupling from BLA-DMS to CeA-DMS (Table A10), when examining the coupling from BLA-DMS to CeA-DMS during lever pressing, the coefficient for x in the control group is negative for all conditions except RR-10, where it turns positive (Table A10, column 3). In contrast, the stress group exhibits the opposite pattern: the coefficient for x is positive for RR-10 but negative for all other conditions. This

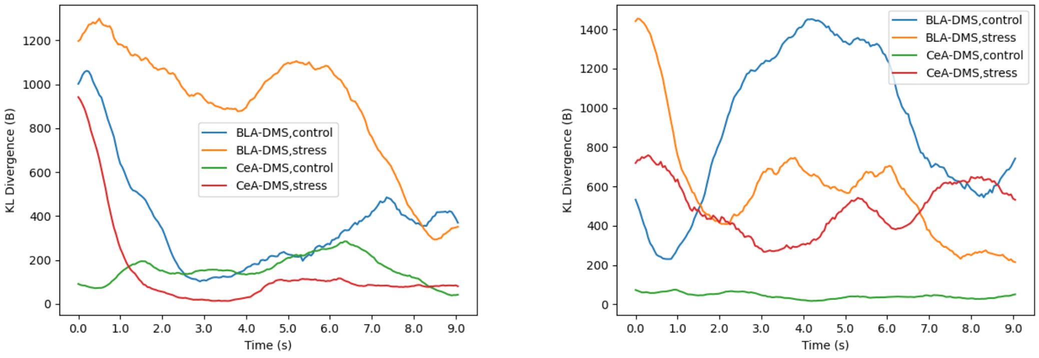

(a) FR-1 (b) RR-2

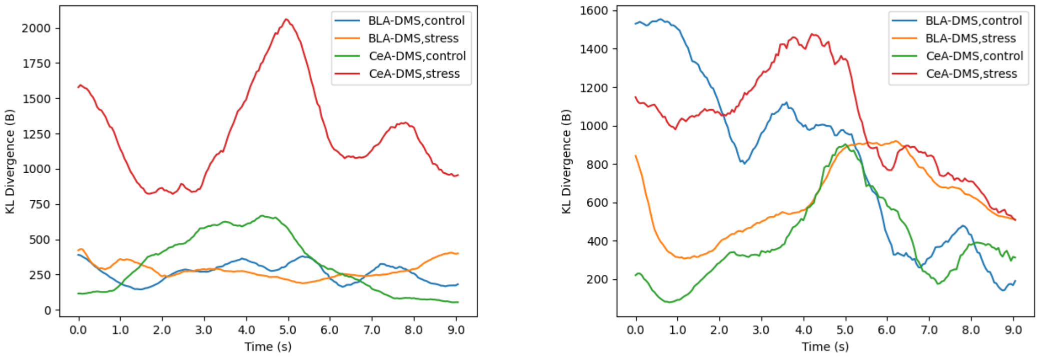

(c) RR-5 (d) RR-10

Figure A4: BLA-DMS and CeA-DMS KL divergence after reward

Table A9: Coefficients of Inter-region Coupling for Each Sessions (Coupling Direction: CeA-DMS to BLA-DMS)

Group	Session	Bout-Intiating Pressing Terms						Reward Terms					
		y	$\dot{y}$	xy	$x\dot{y}$	$\dot{x}y$	$\dot{x}\dot{y}$	y	$\dot{y}$	xy	$x\dot{y}$	$\dot{x}y$	$\dot{x}\dot{y}$
Control	FR-1	-10.9728	-0.086	13.1204	-7.0535	-11.5208	-2.1958	-4.4472	-2.4005	3.7148	2.2945	45.937	1.8896
	RR-2	-39.7674	-5.1685	26.4704	16.6803	-6.7267	0.5072	5.6266	1.8523	-38.8301	-2.9977	5.0702	2.1851
	RR-5	9.0589	-0.0922	21.8115	-38.6233	-1.1861	5.7804	-1.1869	1.8692	-32.7316	-30.9094	-7.5127	-0.2771
	RR-10	-22.4841	-1.8079	15.7239	-20.2152	-33.8723	0.6346	-9.183	-0.6276	-43.7452	8.1389	3.5995	2.3399
Stress	FR-1	-3.8012	4.902	9.4183	10.1017	13.8597	3.468	28.2838	-10.6088	4.4508	-21.4283	-21.9239	-1.984
	RR-2	-21.6682	-0.0382	1.2786	3.1537	7.0109	0.0331	21.3051	6.7219	-8.9069	12.667	0.6839	1.539
	RR-5	0.5445	-4.1176	-4.1945	-12.7811	2.3048	-1.5244	10.9121	2.4969	-12.5218	4.2955	-21.2052	0.3892
	RR-10	-16.1355	-2.2462	-8.5142	-5.7324	-2.7469	-0.2966	-2.7948	11.5953	-11.5981	22.3896	-8.7602	-3.4383

suggests that the information transmitted from the BLA-DMS to the CeA-DMS differs between the two groups, with the direction of the signal being reversed.

During reward delivery, the coefficient for x is generally consistent between the control and stress groups. As uncertainty increases, the sign of the coefficient shifts from positive to negative (Table A10, column 9). In the control group, this shift occurs by RR-2, while in the stress group, it does not happen until RR-5. This indicates that the stress group shows less flexibility in adjusting to reward uncertainty compared to the control group. The dynamics of the $x\dot{y}$, $\dot{x}y$ terms are less clear, as both groups adjust differently depending on the environmental context.

For the control group, the coefficient for xy is negative at RR-2 and RR-5, and positive in other conditions (Table A10, column 5). This suggests that, once uncertainty is introduced, the BLA-DMS in the control group shows a withdrawal response, while the CeA-DMS continues to ”encourage” the pressing behavior. In contrast, the stress group consistently shows positive coefficients for xy, indicating that their BLA-DMS motivation to press the lever remains strong. However, as uncertainty increases, the CeA-DMS in the stress group inhibits the BLA-DMS's motivation to press the lever.

During reward trials, the coefficient for xy in the control group is negative at FR-1, but positive in other conditions . In the stress group, the coefficient is negative only in RR-10, with all other conditions showing positive values (Table A10, column 11). This suggests that certain rewards (FR-1) do not strongly excite the BLA-DMS in the control group, while highly uncertain rewards reduce the BLA-DMS's interest in the stress group. The most exciting reward probability for both groups is RR-2, where the coefficient reaches its maximum, indicating the highest level of excitement.

Table A10: Coefficients of Inter-region Coupling for Each Sessions (Coupling Direction: BLA-DMS to CeA-DMS)

Group	Session	Bout-Intiating Pressing Terms						Reward Terms					
		x	$\dot{x}$	xy	$\dot{x}y$	$x\dot{y}$	$\dot{x}\dot{y}$	x	$\dot{x}$	xy	$\dot{x}y$	$x\dot{y}$	$\dot{x}\dot{y}$
Control	FR-1	6.0227	5.276	18.1119	13.0824	2.6927	-1.5149	3.903	3.0919	-5.3688	4.3428	-13.0175	-0.1266
	RR-2	-6.3681	3.1231	-18.6917	5.2189	13.0405	1.2694	-12.5937	-3.1018	42.763	-10.052	0.4524	-0.1029
	RR-5	-24.3138	-0.6071	-5.6235	-8.3053	9.6923	0.6464	-27.4965	-1.4647	3.8575	24.4247	-11.5234	1.4435
	RR-10	-17.6802	0.3804	9.105	-3.1933	17.3809	1.9187	-18.7925	-1.0901	23.6945	-18.227	3.6905	-1.031
Stress	FR-1	-7.6168	0.8112	15.7285	4.274	-8.9112	-0.6267	1.2134	-1.5246	6.8222	-25.7709	22.0973	-6.6466
	RR-2	-7.3069	0.3715	17.2515	2.5673	-14.4063	-2.1358	19.541	-1.7014	20.7598	21.6013	-5.3767	0.6239
	RR-5	-9.838	-0.5013	10.6379	1.0994	40.8554	1.4808	-9.8796	2.8574	2.0249	-7.3337	-7.4155	-3.3201
	RR-10	5.0276	-0.9859	21.7281	9.3907	13.1481	-3.9621	-51.6268	1.5625	-7.8097	-20.0777	12.1191	-1.2871

A.1.3 Robustness Test

To ensure the statistical robustness and reproducibility of the mechanisms learned by the Unified Coupled System, we conducted a stability analysis using $N = 10$ independent random seeds (specifically, seeds $0, 10, 20, \ldots, 90$).

Table A11 presents the statistical characteristics (Mean, Standard Deviation, Range, and Coefficient of Variation) for both the learned macro-parameters (e.g., Suppression Power, Interaction Scale, etc) and the functional response metrics (e.g., Recovery Time, Max N1 Deviation, etc).

Table A11: Statistical Robustness of Learned Parameters and Functional Metrics Across 10 Independent Seeds

		Control				Stress			
	Parameters	Mean	Standard Error	Range	Coefficient of Variation	Mean	Standard Error	Range	Coefficient of Variation
Training Index	final loss	0.001507	0.000282	[0.001107, 0.002091]	0.1871	0.003581	0.000477	[0.002855, 0.004457]	0.1333
	mse	0.000701	0.000139	[0.000490, 0.000987]	0.1979	0.002735	0.000201	[0.002381, 0.003043]	0.0735
Learned Parameters	interactions cale	0.5186	0.063	[0.4094, 0.6249]	0.1214	0.5182	0.0531	[0.4407, 0.6254]	0.1024
	suppression power	1.2318	0.0795	[1.0965, 1.3718]	0.0645	1.246	0.0591	[1.1563, 1.3519]	0.0474
	BLA-DMS decay modulation	1.7571	0.087	[1.5809, 1.8989]	0.0495	1.5451	0.2172	[1.0864, 1.7548]	0.1405
	CeA-DMS decay modulation	1.7591	0.0421	[1.7027, 1.8405]	0.0239	1.7429	0.0599	[1.6647, 1.8516]	0.0344
	CeA-DMS → BLA-DMS excitatory	0.3634	0.0896	[0.1933, 0.5055]	0.2465	0.3527	0.0987	[0.1995, 0.5364]	0.2798
	CeA-DMS → BLA-DMS inhibitory	0.1234	0.0501	[0.0529, 0.2376]	0.4062	0.1387	0.0468	[0.0804, 0.2549]	0.3375
Response to Perturbation	recovery time	3	0.7746	[2.0000, 4.0000]	0.2582	1	0	[1.0000, 1.0000]	0
	max BLA-DMS deviation	0.3389	0.0688	[0.2373, 0.4416]	0.203	0.057	0.0089	[0.0438, 0.0715]	0.1558
	max CeA-DMS deviation	0.3389	0.0953	[0.1729, 0.4691]	0.2813	0.6698	0.0722	[0.5650, 0.7655]	0.1077
	steady state error	0.0564	0.0041	[0.0510, 0.0619]	0.0724	0.0512	0.0037	[0.0459, 0.0567]	0.0718

The distribution and variability of the learned parameters and functional metrics listed in Table A11 are visually represented by the box plots in Figure A5. Our stability analysis provides insight into the trade-off between stability and flexibility enforced by chronic stress. While the Stress models achieved near-zero CV for Recovery Time, confirming a highly rigid, robust strategy to perturbation, the Control models retained a higher functional CV (e.g., 25.8% CV in Recovery Time). This elevated functional variance in the Control group may be interpreted as a higher degree of behavioral or functional flexibility in response to acute challenges. Furthermore, the highest CVs were observed in the inter-pathway connection weights (CeA-DMS → BLA-DMS coupling), indicating that the system preserves structural flexibility (functional compensation) as a core mechanism for achieving functional stability. This finding supports the idea that the brain does not seek absolute stability ($\text{CV} \ll 0.01$), but rather seeks a balance where core function is preserved while maintaining necessary flexibility for adaptation.

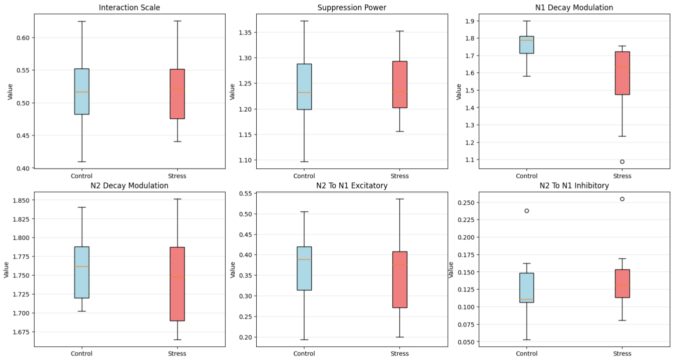

(a) Learned parameters

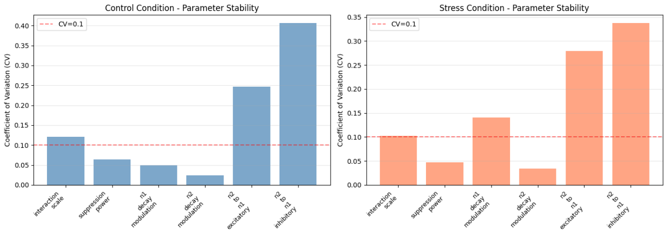

(b) Coefficient if Variation

Figure A5: Robustness test for the ANN model.

A.2 Experiment Description

The dataset provided by the authors comprises behavioral and neural recordings subjected to 14-day chronic unpredictable stress or control handling prior to experiments. At the behavioral level, the dataset includes lever-pressing frequency from a 4-day training protocol (fixed ratio, FR-1, 100% reward probability, to random ratios, RR-2, RR-5, RR-10, averaging 2, 5, and 10 presses per reward) in the Devaluation and Contingency Degradation Experiments, establishing action-outcome learning baselines. On day 5, behavioral flexibility was assessed via the Devaluation test (specific satiety) or Contingency Degradation training (RR-10 vs. RR-10 with 0.1 probability of non-contingent rewards), with the Contingency Degradation test conducted on day 6 (5-min session). At the neural level, GCaMP8s fluorescence time-series data, sampled at 20 Hz (0.05-s intervals) for a 20-second window (±10 s relative to event onset at time 0), were recorded from BLA and CeA neurons projecting to the DMS via AAV-mediated intersectional expression. These data, captured during training, include activity aligned to bout-initiating presses and reward collection, while post-training sessions recorded responses to non-contingent rewards and footshock (Extended Data Fig. 6).

During the 4-day lever-pressing learning, BLA-DMS pathway in control mice exhibits robust activation aligned to reward collection, supporting action-outcome learning and CeA-DMS pathway shows less activity (Fig. 2g). The BLA-DMS pathway in stress mice exhibits less activity while in CeA-DMS pathway it exhibits activation when the probability of reward is low (Fig. 2m). For unexpected stimuli, both pathways display acute activation in response to footshock in both control and stress groups, indicating similar responses (Extended Data Fig. 6e, 6h). In contrast, unpredicted reward delivery elicits sustained CeA-DMS excitation in stressed mice, unlike the transient BLA-DMS response in controls (Extended Data Fig. 6a, 6c). These signal changes were quantified using the Area Under the Curve (AUC) method for 3-s periods post-reward or 1-s post-shock, revealing group-specific differences (Extended Data Fig. 6).

Because the signal might start to deviate from the original mean value shortly before the stimulus due to psychological activity in anticipation of the event, we choose to use the data from -10 to -1 seconds as the baseline. This period captures the signal immediately prior to the stimulus, while avoiding the last second (-1 to 0 seconds), which may show changes due to anticipatory responses.

A.3 Kullback-Leibler Divergence

Kullback-Leibler (KL) divergence (D_{KL}) measures the difference in information content between two probability distributions. Derived from relative entropy, KL divergence quantifies the difference between two distributions as follows:

$$D_{KL}(P_b||P_a) = \frac{1}{\ln 2}\int_{-\infty}^{\infty} dx P_b(x)(\ln P_b(x) - \ln P_a(x)) \tag{A.1}$$

where $P_b(x)$ and $P_a(x)$ denote the probability density functions. The term $\ln 2$is included to express the divergence in bits (the dimension of information). If the event-related distributions are identical, the KL divergence is zero. If $P_a(x)$ is

$$P_a(x) = \frac{1}{\sigma_a\sqrt{2\pi}}e^{-\frac{(x-\mu_a)}{2\sigma_a^2}} \tag{A.2}$$

and $P_b(x)$ is

$$P_b(x) = \frac{1}{\sigma_b\sqrt{2\pi}}e^{-\frac{(x-\mu_b)}{2\sigma_b^2}} \tag{A.3}$$

in which μ_a and μ_b are the means, and σ_a and σ_b are the standard deviations of the two distributions. The KL divergence $D_{KL}(P_b||P_a)$ between two normal distributions $P_a(x)$ and $P_b(x)$ is given by:

$$D_{KL}(P_b||P_a) = F(x)|_{x=\infty} - F(x)|_{x=-\infty} \tag{A.4}$$

in which $F(x)$ is

$$\begin{aligned} F(x) \quad = \quad & \frac{1}{\ln 2}\frac{e^{-\frac{(x-\mu_b)^2}{2\sigma_a^2}}}{4\sqrt{2\pi}\sigma_a^2\sigma_b^2} \\ & \times(-2\sigma_a(\mu_b - x)(\sigma_b^2 - \sigma_a^2) \\ & +\sqrt{2\pi}e^{\frac{(\mu_b-x)^2}{(2\sigma_a^2)}}\operatorname{erf}[\frac{\mu_b - x}{\sqrt{2}\sigma_a}] \\ & \times(-(\sigma_a^2 - \sigma_b^2)(\sigma_a^2 - (\mu_b - x)^2) - 2\sigma_a^2\sigma_b^2\ln[\frac{e^{1/2(-\frac{(\mu_b-x)^2}{\sigma_a^2}+\frac{(u2-x)^2}{\sigma_b^2})}\sigma_b}{\sigma_a}])) \end{aligned} \tag{A.5}$$

where erf[.] is the error function, defined as:

$$\operatorname{erf}[x] = \frac{2}{\pi}\int_{-\infty}^{x} e^{-t^2}dt \tag{A.6}$$

One can check that when the KL divergence D_1 is computed the case where $\mu_a = \mu_b$ and $\sigma_a = \sigma_b \pm n$, and D_2 is computed for the case where $\mu_a = \mu_b \pm n$ and $\sigma_a = \sigma_b$ (n is real number), we have quite often $D_1 < D_2$. This suggests that differences in the means of the distributions tend to produce larger KL divergence values, while differences in standard deviations result in a smaller KL divergence unless the standard deviation disparity is very large.

To compare the distribution of a time series with the baseline time series, we can apply a sliding window method to observe changes in the KL divergence over time. Using a 1-second time window, we sample the data every second. For each window, we reshape the distribution function using kernel density estimation (via the scipy.stats library, gaussian_kde), and then compute the KL divergence at each time step.

Since the scale of KL divergence is the same as entropy, it can be used to estimate the energy of the information. The KL divergence $D_{KL}(P_b||P_a)$ at each time step represents the information difference between the baseline and the observed signal. The total information quantity I can be estimated by summing the KL divergences over time:

$$I = \sum_{i=1}^{N} D_{KL}(P_b||P_a)(t_i) \tag{A.7}$$

This quantity gives a measure of the information accumulated over the time series.

A.4 Baseline and Standard Deviation Before and After Perturbation

The baseline means and variances before and after various perturbations and stimuli are summarized in Tables A12 and A13. The pre-perturbation baseline was calculated as the mean and variance of the 9-second segment immediately preceding the onset of the perturbation. The post-perturbation baseline was computed using data starting 5 seconds after the perturbation onset. This approach minimizes the influence of perturbation-related transient responses on the estimation of the true baseline.

Table A12: Mean and Standard Deviation Before and After Perturbation for Each Group and Pathway

Case	Group	Pathway	Before Perturbation		After Perturbation	
			Mean	Standard Deviation	Mean	Standard Deviation
FootShock	Control	BLA-DMS	0.0252	0.3495	-0.397	0.4327
		CeA-DMS	0.2392	0.3712	-0.3924	0.5516
	Stress	BLA-DMS	0.2294	0.3453	-0.6465	0.4337
		CeA-DMS	0.1392	0.3858	-0.1597	0.655
Unpredicted Reward	Control	BLA-DMS	0.0474	0.2868	0.0331	0.4192
		CeA-DMS	0.0849	0.2443	-0.1326	0.5861
	Stress	BLA-DMS	0.1182	0.2907	-0.3153	0.5291
		CeA-DMS	-0.1213	0.3819	0.5462	0.436

Table A13: Mean and Standard Deviation Before and After Perturbation for Each Group, Pathway and Sessions

			Bout-Initiating Presses				Reward			
Group	Pathway	Session	Before Perturbation		After Perturbation		Before Perturbation		After Perturbation	
			Mean	Standard Deviation	Mean	Standard Deviation	Mean	Standard Deviation	Mean	Standard Deviation
Control	BLA-DMS	FR-1	-0.1646	0.273	0.0276	0.3599	-0.1148	0.3286	0.0013	0.5163
		RR-2	0.0396	0.3091	0.1811	0.5335	0.0612	0.317	0.0177	0.5781
		RR-5	-0.0949	0.2009	0.0239	0.3012	-0.1299	0.2749	-0.0006	0.4203
		RR-10	-0.0327	0.2788	-0.0599	0.3453	-0.1798	0.259	0.0033	0.43
	CeA-DMS	FR-1	-0.1787	0.4134	-0.2178	0.4639	-0.1696	0.2589	-0.1512	0.4079
		RR-2	-0.0686	0.2367	-0.2642	0.3378	-0.1929	0.3713	-0.0913	0.4067
		RR-5	-0.0531	0.2112	-0.1903	0.3328	-0.0859	0.2628	0.0034	0.3829
		RR-10	-0.0401	0.2659	-0.1484	0.3567	-0.174	0.2733	-0.0149	0.4906
Stress	BLA-DMS	FR-1	-0.0477	0.2545	-0.4853	0.2363	-0.1056	0.2504	-0.5228	0.39
		RR-2	-0.0977	0.3392	-0.5101	0.3448	-0.1962	0.346	-0.4532	0.3779
		RR-5	-0.1946	0.2426	-0.4142	0.4051	-0.2327	0.2769	-0.3854	0.4245
		RR-10	-0.0601	0.2117	-0.3598	0.4095	-0.1126	0.2546	-0.3761	0.4283
	CeA-DMS	FR-1	-0.079	0.2885	-0.0084	0.2949	-0.0623	0.2761	0.0746	0.2255
		RR-2	-0.1014	0.2535	0.0244	0.3791	-0.2146	0.2228	0.1005	0.3762
		RR-5	-0.1004	0.2245	0.1262	0.2934	-0.1458	0.2221	0.2809	0.3931
		RR-10	-0.0586	0.2616	0.1567	0.3645	-0.0959	0.2289	0.3647	0.2996

A.5 Single Variable Model Constructed by Ridged Regression

The experiments can be viewed as perturbations to the system. Before the perturbation, the signals are in a steady state; after the perturbation, the system returns to a steady state that is near the original one. This process can be roughly modeled as a damping system, where the signals follow a damping equation:

$$\ddot{x} = a_0 + a_1 x + a_2 \dot{x} + a_3 x^2 + a_4 \dot{x}^2 + a_5 x \dot{x} + H.O.T \tag{A.8}$$

In this equation, x represents the signal recorded in the experimental data, and $\dot{x}$ can be estimated as the difference between consecutive data points, i.e., $x_t - x_{t+1}$. The acceleration $\ddot{x}$ takes the form of a damping recovery equation. To construct this model, we apply ridge regression (python sklearn library, Ridge packet). The term $H.O.T$ represents higher-order terms, which account for nonlinearities but contribute less significantly to the overall dynamics.

When $a_3 < 0$ and all other constants are zero, the model reduces to a harmonic oscillation. The damping model (A.8) can be rewritten as a system of first-order differential equations:

$$\begin{aligned} \dot{x} &= v \\ \dot{v} &= a_0 + a_1 x + a_2 v + a_3 x^2 + a_4 v^2 + a_5 x v \end{aligned} \tag{A.9}$$

The behavior of the system can be analyzed by examining the Jacobian matrix around the steady state, according to the theory of ordinary differential equation. The Jacobian (J) is given by:

$$J = \begin{pmatrix} 0 & 1 \\ a_1 + 2a_3 x + a_5 v & a_2 + 2a_4 v + a_5 x \end{pmatrix}_{x=x_s, v=\dot{x}_s} \tag{A.10}$$

In this equation, the steady state x_s is determined by the mean value of the signal during the last 5 seconds of the recording, so $\dot{x}_s = 0$. Therefore, the Jacobian simplifies to:

$$J = \begin{pmatrix} 0 & 1 \\ a_1 + 2a_3 x & a_2 + a_5 x \end{pmatrix}_{x=x_s} \tag{A.11}$$

The stability of the system around the steady state is determined by the eigenvalues of the Jacobian. If the real parts of all the eigenvalues are negative, the system is stable around the steady state. This simplified model neglects any oscillations or fluctuations around the steady state.

The single variable model constructed via ridge regression for the signal strength after perturbation is summarized in Tables A14 and A15. The coefficients obtained from the regression are used in the Jacobian calculation to analyze the stability characteristics of the signal pathways.

Table A14: Single Variable Model for Footshock and Unpredicted Reward

Case	Group	Pathway	Model
FootShock	Control	BLA-DMS	$-1.9228 - 5.3333x - 27.5758\dot{x} - 6.7222x^2 - 0.7575x\dot{x} + 0.2688\dot{x}^2$
		CeA-DMS	$-6.7536 - 6.3322x - 28.2132\dot{x} + 7.1175x^2 + 4.2315x\dot{x} + 0.9127\dot{x}^2$
	Stress	BLA-DMS	$-9.5841 - 7.4973x - 25.8458\dot{x} + 11.8622x^2 + 3.5148x\dot{x} + 0.1518\dot{x}^2$
		CeA-DMS	$-5.4493 - 6.1680x - 26.8525\dot{x} + 2.6939x^2 + 1.7576x\dot{x} + 1.5371\dot{x}^2$
Unpredicted Reward	Control	BLA-DMS	$4.4350 - 41.7119x - 29.2815\dot{x} + 1.4989x^2 + 1.8050x\dot{x} - 0.5230\dot{x}^2$
		CeA-DMS	$-6.0246 - 47.8635x - 29.5425\dot{x} + 4.4658x^2 - 0.4575x\dot{x} + 0.5643\dot{x}^2$
	Stress	BLA-DMS	$-13.5982 - 31.6003x - 26.9727\dot{x} + 23.4829x^2 + 6.3679x\dot{x} + 0.7245\dot{x}^2$
		CeA-DMS	$12.6666 - 11.6088x - 22.5005\dot{x} - 13.6021x^2 - 8.2384x\dot{x} - 1.8809\dot{x}^2$

Table A15: Single Variable Model for Each Sessions

			Session	Model
Bout-Initiating Press	BLA-DMS	Control	FR-1	$0.8080 - 15.7358x - 23.5192\dot{x} - 3.8052x^2 - 11.5183x\dot{x} - 0.8064\dot{x}^2$
			RR-2	$4.4862 - 21.2023x - 27.1370\dot{x} - 8.8273x^2 - 0.4566x\dot{x} - 0.4655\dot{x}^2$
			RR-5	$2.2484 - 14.9366x - 25.7808\dot{x} - 1.7498x^2 - 3.3393x\dot{x} - 4.4578\dot{x}^2$
			RR-10	$0.5783 - 20.1005x - 26.3607\dot{x} - 0.5587x^2 - 2.3977x\dot{x} - 0.8145\dot{x}^2$
		Stress	FR-1	$-2.8722 - 4.8894x - 26.5331\dot{x} + 5.4166x^2 + 4.1365x\dot{x} - 4.2691\dot{x}^2$
			RR-2	$-4.5259 - 5.2008x - 23.6132\dot{x} + 6.1047x^2 + 8.2456x\dot{x} + 1.5934\dot{x}^2$
			RR-5	$-8.8918 - 16.7709x - 25.2816\dot{x} + 13.9339x^2 + 7.6560x\dot{x} - 0.5234\dot{x}^2$
			RR-10	$-5.9443 - 12.6286x - 24.7817\dot{x} + 8.5313x^2 + 8.6004x\dot{x} + 0.9931\dot{x}^2$
	CeA-DMS	Control	FR-1	$-7.3974 - 37.2653x - 23.5145\dot{x} + 18.5044x^2 + 20.6785x\dot{x} - 1.8446\dot{x}^2$
			RR-2	$-6.6367 - 24.5748x - 26.2639\dot{x} + 10.4547x^2 + 7.4137x\dot{x} - 1.6937\dot{x}^2$
			RR-5	$-3.8252 - 15.2978x - 29.1488\dot{x} + 3.8441x^2 + 2.6711x\dot{x} + 2.3924\dot{x}^2$
			RR-10	$-4.6397 - 20.4565x - 29.4115\dot{x} + 5.9655x^2 + 0.3358x\dot{x} + 1.2348\dot{x}^2$
		Stress	FR-1	$-0.1629 - 15.7361x - 28.7432\dot{x} + 0.7284x^2 + 0.4776x\dot{x} - 0.0127)\dot{x}^2$
			RR-2	$0.3624 - 9.8587x - 28.4398\dot{x} - 0.9916x^2 + 2.0545x\dot{x} + 0.3305\dot{x}^2$
			RR-5	$2.6053 - 21.6849x - 26.7041\dot{x} - 4.9936x^2 - 4.4751x\dot{x} + 0.5131\dot{x}^2$
			RR-10	$3.4412 - 17.3493x - 27.4089\dot{x} - 5.7710x^2 - 5.4578x\dot{x} - 1.3017\dot{x}^2$
Reward	BLA-DMS	Control	FR-1	$-1.1611 - 10.5803x - 28.0988\dot{x} + 4.2600x^2 + 7.1836x\dot{x} + 1.5830\dot{x}^2$
			RR-2	$1.3650 - 17.8102x - 26.0477\dot{x} + 5.9901x^2 - 2.4885x\dot{x} - 1.7515\dot{x}^2$
			RR-5	$0.8125 - 17.5678x - 27.2602\dot{x} + 1.2080x^2 + 0.2912x\dot{x} - 0.7876\dot{x}^2$
			RR-10	$0.3000 - 23.0053x - 27.5599\dot{x} + 5.3115x^2 + 3.783)x\dot{x} - 0.5757\dot{x}^2$
		Stress	FR-1	$-7.0527 - 7.0785x - 18.5046\dot{x} + 7.5655x^2 + 13.3272x\dot{x} + 1.1170\dot{x}^2$
			RR-2	$-6.9404 - 8.3674x - 22.9869\dot{x} + 8.5527x^2 + 10.4850x\dot{x} + 1.9020\dot{x}^2$
			RR-5	$-6.8373 - 10.4463x - 26.1416\dot{x} + 10.7682x^2 + 1.4656x\dot{x} + 1.2076\dot{x}^2$
			RR-10	$-5.8683 - 11.5925x - 21.3650\dot{x} + 9.7149x^2 + 10.8210x\dot{x} - 0.7781\dot{x}^2$
	CeA-DMS	Control	FR-1	$-2.6936 - 18.6995x - 29.3507\dot{x} + 5.5133x^2 - 0.5891x\dot{x} - 0.4534\dot{x}^2$
			RR-2	$0.0812 + -16.1880x - 27.0680\dot{x} + 0.3862x^2 - 1.6093x\dot{x} - 2.2298)\dot{x}^2$
			RR-5	$-0.4529 - 8.0630x - 29.1202\dot{x} + 0.6791x^2 - 0.3790x\dot{x} + 1.0850\dot{x}^2$
			RR-10	$-0.4544 - 16.4115x - 29.9136\dot{x} + 0.2461x^2 - 2.5416)x\dot{x} - 0.1144\dot{x}^2$
		Stress	FR-1	$-0.1809 - 14.3627x - 28.0888\dot{x} - 3.4829x^2 - 3.1300x\dot{x} + 1.1113\dot{x}^2$
			RR-2	$2.0181 - 17.8495x - 27.8350\dot{x} - 0.5715x^2 - 4.2789x\dot{x} - 0.7502\dot{x}^2$
			RR-5	$3.0939 - 11.5079x - 28.2409\dot{x} - 5.8617x^2 - 4.1339x\dot{x} + 0.3992\dot{x}^2$
			RR-10	$12.9137 - 24.3802x - 25.5777\dot{x} - 18.7923x^2 - 3.9101x\dot{x} - 1.3164\dot{x}^2$

A.6 Coupling Model for Pathway Interactions

The authors did not specifically point out whether the signals from the two pathways in the same group were observed simultaneously. However, since the number of mice involved in each pathway are different, we can deduce that the signals were not observed synchronously. Thus, causality analysis by transfer entropy, which relies on synchronous time-series data, cannot be applied. To explore whether there is a profound coupling between the two pathways, defined by nonlinear interactions, we use a coupling model.

Our approach is based on the assumption that, although the data from different mice are not temporally synchronized, the underlying dynamical rules and interaction patterns of the neural circuits are reproducible under identical experimental conditions. The Ridge Regression coupling model we use is designed to capture this non-synchronous coupling.

This coupling model is an extension of the damping model (A.8). Let x represent the signal detected by the BLA-DMS pathway and y the signal from the CeA-DMS pathway. The model accounts for both the self-dynamics and cross-dynamics between the two pathways. The equations for each pathway are:

$$\ddot{x} = a_0 + a_1 x + a_2 \dot{x} + a_3 x^2 + a_4 \dot{x}^2 + a_5 x\dot{x} + b_1 y + b_2 \dot{y} + b_3 xy + b_4 x\dot{y} + b_5 \dot{x}y + b_6 \dot{x}\dot{y} + H.O.T \tag{A.12}$$

$$\ddot{y} = c_0 + c_1 y + c_2 \dot{y} + c_3 y^2 + c_4 \dot{y}^2 + c_5 y\dot{y} + d_1 x + d_2 \dot{x} + d_3 xy + d_4 y\dot{x} + d_5 \dot{y}x + d_6 \dot{x}\dot{y} + H.O.T \tag{A.13}$$

The coefficients a and c (from 0 to 5) represent the self-dynamics of each pathway, while b and d (from 1 to 6) represent the coupling and nonlinear interactions between the two pathways. By including both the intrinsic dynamics of each pathway and the nonlinear influence of the other, the model quantifies how one pathway's behavior is affected by the other's.

This model is not designed for superior predictive accuracy, but rather to serve as an analytical tool that allows us to explore and quantify the nonlinear interactions between the two pathways under identical experimental conditions. The key contribution of the model lies in its ability to reveal the adaptive regulatory mechanisms of the neural circuits, as we compare the changes in coupling coefficients (b and d) across different experimental conditions (e.g., control vs. stress).

The coupled models, constructed through ridge regression for the signal strength during footshock and unpredicted reward, is summarized in Table A16. The coefficients are used to evaluate the interaction between the pathways. Since the model follows the same structure for all sessions, and the number of sessions is large, we have simplified the representation by showing only the coefficients of the model in Table A17 to improve readability.

Table A16: Coupling Model for Footshock and Unpredicted Reward

Case	Group	Pathway	Model
FootShock	Control	BLA-DMS	$\ddot{x} = -28 - 179.05x - 35.65\dot{x} - 43.29x^2 - 23.16x\dot{x} - 0.6\dot{x}^2 + 126.48y + 2.61\dot{y} + 70.67xy + 7.7x\dot{y} + 19.93\dot{x}y + 0.67\dot{x}\dot{y}$
		CeA-DMS	$\ddot{y} = 5.23 - 69.93y - 27.55\dot{y} - 54.20y^2 - 26.55y\dot{y} - 0.11\dot{y}^2 + 90.84x + 1.59\dot{x} + 63.55xy + 2.80\dot{x}y + 34.01x\dot{y} + \dot{x}\dot{y}$
	Stress	BLA-DMS	$\ddot{x} = -25.82 - 6.79x - 29.28\dot{x} + 57.56x^2 + 1.34x\dot{x} - 0.09\dot{x}^2 + 7.63y + 1.62\dot{y} - 24.78xy + 4.5x\dot{y} + 1.61\dot{x}y + 1.23\dot{x}\dot{y}$
		CeA-DMS	$\ddot{y} = 31.56 - 66.03y - 25.53\dot{y} + 33.53y^2 + 0.16y\dot{y} - 0.22\dot{y}^2 + 61.99x - 0.01\dot{x} - 46.15xy + 7.65\dot{x}y + 7.80x\dot{y} + 0.87\dot{x}\dot{y}$
Unpredicted Reward	Control	BLA-DMS	$\ddot{x} = 15.86 - 97.79x - 33.95\dot{x} - 25.61x^2 + 13.37x\dot{x} + 0.26\dot{x}^2 + 75.20y + 2.34\dot{y} + 83.57xy - 0.81x\dot{y} - 16.29\dot{x}y + 0.85\dot{x}\dot{y}$
		CeA-DMS	$\ddot{y} = -16.02 - 108.27y - 31.04\dot{y} + 2.06y^2 + 1.56y\dot{y} + 0.57\dot{y}^2 + 48.17x + 0.32\dot{x} + 5.76xy - 5.56y\dot{x} - 0.49\dot{y}x + 0.35\dot{x}\dot{y}$
	Stress	BLA-DMS	$\ddot{x} = -5.75 - 13.10x - 20.76\dot{x} + 71.28x^2 + 2.8x\dot{x} + 0.44\dot{x}^2 - 22.14y + 5.11\dot{y} - 30.70xy + 14.95x\dot{y} - 14.55\dot{x}y - 1.06\dot{x}\dot{y}$
		CeA-DMS	$\ddot{y} = 21.64 - 14.46y - 26.82\dot{y} - 17.55y^2 - 5.38y\dot{y} - 1.90\dot{y}^2 + 17.93x + 0.71\dot{x} + 2.54xy + 0.74y\dot{x} - 7.11\dot{y}x - 1.67\dot{x}\dot{y}$

Table A17: Coefficients of Coupling Pathways in Each Sessions

Session		Bout-Intiating Pressing		Reward			Bout-Intiating Pressing		Reward	
		BLA-DMS					CeA-DMS			
	Terms	Control	Stress	Control	Stress	Terms	Control	Stress	Control	Stress
FR-1	Intercept	-1.2489	-2.1823	-1.86	-12.616	Intercept	-16.8069	-3.8873	-8.8254	1.0603
	x	-26.9824	1.8739	-22.2405	-9.3874	y	-72.2964	-32.7534	-61.9376	-18.4418
	$\dot{x}$	-26.7644	-28.8582	-21.9967	-13.2609	$\dot{y}$	-19.8153	-33.155	-30.4395	-15.7282
	x^2	-59.1012	17.0135	41.835	20.0986	y^2	35.4503	1.4723	18.1112	-33.7282
	$x\dot{x}$	-31.1631	-1.6622	8.4666	24.6131	$y\dot{y}$	38.7026	3.5083	-7.141	-11.7215
	$\dot{x}^2$	-1.4997	-4.8887	1.5227	2.2802	$\dot{y}^2$	-1.4352	0.1461	-1.0233	1.1328
	y	-10.9728	-3.8012	-4.4472	28.2838	x	6.0227	-7.6168	3.903	1.2134
	$\dot{y}$	-0.086	4.902	-2.4005	-10.6088	$\dot{x}$	5.276	0.8112	3.0919	-1.5246
	xy	13.1204	9.4183	3.7148	4.4508	xy	18.1119	15.7285	-5.3688	6.8222
	$x\dot{y}$	-7.0535	10.1017	2.2945	-21.4283	$\dot{x}y$	13.0824	4.274	4.3428	-25.7709
	$\dot{x}y$	-11.5208	13.8597	45.937	-21.9239	$x\dot{y}$	2.6927	-8.9112	-13.0175	22.0973
	$\dot{x}\dot{y}$	-2.1958	3.468	1.8896	-1.984	$\dot{x}\dot{y}$	-1.5149	-0.6267	-0.1266	-6.6466
RR-2	Intercept	0.6885	-10.471	2.9059	-16.4149	Intercept	-14.1659	-3.3675	-4.8619	13.0781
	x	-48.0803	-8.8081	-47.543	-19.127	y	-50.1375	-21.2365	-63.6587	-32.0055
	$\dot{x}$	-29.7722	-25.5624	-25.9124	-24.4897	$\dot{y}$	-32.1387	-36.1868	-29.4183	-31.6626
	x^2	-31.0671	23.7959	42.7102	19.3915	y^2	32.0372	-20.5212	-4.7251	-14.256
	$x\dot{x}$	-1.7915	5.5215	0.9906	9.5222	$y\dot{y}$	-1.1266	-9.3956	-7.6634	-2.5822
	$\dot{x}^2$	-0.3429	1.1406	-1.1864	1.9161	$\dot{y}^2$	-2.3155	0.6085	-1.8695	-0.7178
	y	-39.7674	-21.6682	5.6266	21.3051	x	-6.3681	-7.3069	-12.5937	19.541
	$\dot{y}$	-5.1685	-0.0382	1.8523	6.7219	$\dot{x}$	3.1231	0.3715	-3.1018	-1.7014
	xy	26.4704	1.2786	-38.8301	-8.9069	xy	-18.6917	17.2515	42.763	20.7598
	$x\dot{y}$	16.6803	3.1537	-2.9977	12.667	$\dot{x}y$	5.2189	2.5673	-10.052	21.6013
	$\dot{x}y$	-6.7267	7.0109	5.0702	0.6839	$x\dot{y}$	13.0405	-14.4063	0.4524	-5.3767
	$\dot{x}\dot{y}$	0.5072	0.0331	2.1851	1.539	$\dot{x}\dot{y}$	1.2694	-2.1358	-0.1029	0.6239
RR-5	Intercept	3.8787	-27.1371	0.9293	-13.7276	Intercept	-9.007	0.1572	-0.6889	0.0996
	x	-22.2771	-49.2653	-39.3229	-10.124	y	-46.6596	-30.4341	-24.0414	-14.5152
	$\dot{x}$	-26.2183	-31.7039	-28.1359	-27.2299	$\dot{y}$	-30.5187	-11.1559	-30.1862	-32.3312
	x^2	-22.6223	42.556	25.2605	28.5888	y^2	13.9854	-45.2358	13.9694	-13.5299
	$x\dot{x}$	-27.5551	-3.3093	0.1541	-10.7613	$y\dot{y}$	4.3074	-6.2106	-14.8553	-1.8094
	$\dot{x}^2$	-5.0061	-0.9601	-0.592	0.9153	$\dot{y}^2$	2.2272	0.8139	0.4544	0.6211
	y	9.0589	0.5445	-1.1869	10.9121	x	-24.3138	-9.838	-27.4965	-9.8796
	$\dot{y}$	-0.0922	-4.1176	1.8692	2.4969	$\dot{x}$	-0.6071	-0.5013	-1.4647	2.8574
	xy	21.8115	-4.1945	-32.7316	-12.5218	xy	-5.6235	10.6379	3.8575	2.0249
	$x\dot{y}$	-38.6233	-12.7811	-30.9094	4.2955	$\dot{x}y$	-8.3053	1.0994	24.4247	-7.3337
	$\dot{x}y$	-1.1861	2.3048	-7.5127	-21.2052	$x\dot{y}$	9.6923	40.8554	-11.5234	-7.4155
	$\dot{x}\dot{y}$	5.7804	-1.5244	-0.2771	0.3892	$\dot{x}\dot{y}$	0.6464	1.4808	1.4435	-3.3201
RR-10	Intercept	-3.4841	-16.2421	-0.6671	-11.2201	Intercept	-10.9023	6.7196	-2.0642	4.7305
	x	-41.7199	-39.3973	-54.0433	-18.2793	y	-53.9165	-16.3966	-41.3833	-53.0589
	$\dot{x}$	-32.7106	-27.6476	-28.4571	-13.2547	$\dot{y}$	-27.6001	-24.5726	-30.8027	-28.3805
	x^2	-12.8763	30.4992	46.5367	21.3762	y^2	16.1924	-45.7105	17.1295	-42.522
	$x\dot{x}$	-26.9791	4.1615	11.6105	22.6796	$y\dot{y}$	12.8705	-0.1453	-2.9349	12.0812
	$\dot{x}^2$	-1.6542	0.8291	-0.3321	-0.9049	$\dot{y}^2$	1.3191	-0.9394	0.1672	-0.6414
	y	-22.4841	-16.1355	-9.183	-2.7948	x	-17.6802	5.0276	-18.7925	-51.6268
	$\dot{y}$	-1.8079	-2.2462	-0.6276	11.5953	$\dot{x}$	0.3804	-0.9859	-1.0901	1.5625
	xy	15.7239	-8.5142	-43.7452	-11.5981	xy	9.105	21.7281	23.6945	-7.8097
	$x\dot{y}$	-20.2152	-5.7324	8.1389	22.3896	$\dot{x}y$	-3.1933	9.3907	-18.227	-20.0777
	$\dot{x}y$	-33.8723	-2.7469	3.5995	-8.7602	$x\dot{y}$	17.3809	13.1481	3.6905	12.1191
	$\dot{x}\dot{y}$	0.6346	-0.2966	2.3399	-3.4383	$\dot{x}\dot{y}$	1.9187	-3.9621	-1.031	-1.2871

A.7 KL Divergence Between Control and Stress Groups Pre- and Post-Stimulus Onset

The KL divergence between control and stress groups pre- and post- stimulus onset are shown in Table A18. We compute the Kullback-Leibler (KL) divergence by comparing the sequences of the stress group with the control group, using the onset of the stimulus (footshock or unpredicted reward) as a dividing point. Specifically, we calculate the KL divergence between the stress and control group sequences before the stimulus onset, and then calculate the KL divergence between the stress and control group sequences after the stimulus onset.

Table A18 shows that in the CeA-DMS pathway, before the stimulus of an unpredicted reward, the

KL divergence is larger compared to other pathways or conditions. This indicates that before stimuli the difference in the CeA-DMS pathway is more pronounced. Perhaps, in contrast to the footshock, the reward is already anticipated, as discussed in section 2.1. The CeA-DMS is already in a preparatory state, which reflects a difference in the control and stress groups prepare for the stimulus. After the stimulus, the KL divergence in both pathways is larger for the unpredicted reward condition than for the footshock condition. This suggests that the stress group's response to footshock is similar to the control group's response, but different from their response to an unpredicted reward.

Table A18: KL Divergence Between Stress and Control Groups Pre- and Post-Stimulus Onset

	Before Stimulus		After Stimulus	
Pathway	FootShock	Unpredicted Reward	FootShock	Unpredicted Reward
BLA-DMS	89.5149	16.4670	42.4657	329.4257
CeA-DMS	28.5197	200.6111	11.2317	227.6856

A.8 Fourier Analysis Before Footshock

We hypothesize that, prior to the footshock, the signals in the BLA-DMS and CeA-DMS pathways are the most similar to the baseline signals of the rats, as they are not influenced by prior training or expectations of a food reward. This is particularly evident in the control group. Therefore, we perform a frequency domain analysis (Fourier analysis) on the pre-footshock sequences to examine the proportion of dominant rhythms throughout the sequence.

The time series length covers 10 seconds, with a sampling rate of 20 Hz. Table A19 shows the ratios of the top 3 amplitudes for the control group, while Table A20 presents the corresponding ratios for the stress group. The sum of the top 3 amplitudes for the control group is less than 40%, whereas for the stress group, it is less than 60%. This suggests that both the control and stress groups exhibit complex networks formed by the CeA-DMS and BLA-DMS pathways. Specifically, the control group exhibits a more complex network, indicating greater flexibility compared to the stress group.

Table A19: Periods Corresponding to the Top 3 Dominant Amplitudes by Fourier Analysis, Control Group

Pathway	Top 1		Top 2		Top 3	
	Period(s)	Ratio(%)	Period(s)	Ratio(%)	Period(s)	Ratio(%)
BLA-DMS	5.00	14.75	2.00	7.95	1.25	5.55
CeA-DMS	3.33	14.44	5.00	13.08	10.0	9.02

Table A20: Periods Corresponding to the Top 3 Dominant Amplitudes by Fourier Analysis, Stress Group

Pathway	Top 1		Top 2		Top 3	
	Period(s)	Ratio(%)	Period(s)	Ratio(%)	Period(s)	Ratio(%)
BLA-DMS	10.0	28.14	2.50	15.18	5.00	14.15
CeA-DMS	5.00	15.72	10.0	9.49	1.67	7.30

A.9 Neural Network Model Architecture

The simulation by the artificial neural network consists of two independent LSTM networks, x for BLA-DMS pathway and y for CeA-DMS pathway. The choice of LSTM is due to its built-in memory unit (Cell State) and gating mechanisms. These features enable the network to capture the temporal dependencies and persistence of neural activity. When subjected to external perturbations, the network outputs ($x(t)$ and $y(t)$) exhibit an instantaneous increase (response) followed by an exponential decay (returning to baseline), which aligns with the temporal dynamics observed in real neural pathways.

The x network is characterized by low capacity and high sensitivity, responsible for quickly adapting to and precisely predicting environmental signals. The y network, on the other hand, is characterized by high capacity and robustness, and is responsible for maintaining the global state, buffering stress, and exerting inhibitory control over the x network. This design choice stems from our data analysis, which revealed that when an unexpected perturbation occurs, the BLA-DMS pathway's signal tends to destabilize. However, despite this, the overall network does not collapse, as the mice exposed to stressful conditions are still able to complete the task.

Main components of the neural network model are shown in Table A21. There are 7 statistical features of the input signal and target signals to gain "outside" the neural network model. The features of input signals include mean, standard deviation, skewness, kurtosis are used for the parameter predictor to judge whether the system is exposed in chronic stress environment. The statistical difference of input signals and the target signals are taking into account by the neural network to judge whether the optimization reaches the aim.

Table A21: Model Components

Components	Class	Input Dimension	Hidden Dimension	Output Dimension	Key Functions
Parameter Predictor	Feedforward Neural Networks	7 (statistical feature)	64	6 (ϕ)	Predict system's macroscopic parameters
x (BLA-DMS)	Adaptive LSTM Predictor	1 (signal)	32	1 (output)	exploration_bias $= 0.2$
y CeA-DMS	Adaptive LSTM Predictor	1 (signal)	32	1 (output)	exploration_bias $= -1$
x/y LSTM core	LSTM	1	32	32 (hidden)	Predict internal state of baseline signal
x/y predictor	Linear Layer	32 (hidden)	-	1	Predict baseline signal
x/y threshold net	Feedforward Neural Networks	33 (hidden+1)	16	1 (base threshold)	Predict baseline of dynamical threshold
x/y weight net	Feedforward Neural Networks	33 (hidden+1)	16	1 (base weight)	Predict baseline weights of bias signal

The macroscopic parameters (ϕ) are used to represent the interaction scale and nonlinearity of the system consisted by x and y nets, the decay modulation of x and y nets, the excitation and inhibition of y to x net. These parameters are figure out by parameter predictor. The key algorithm of this component is in Algorithm 1. The input variables are from the statistical feature component which forms a R^7 Euclidean space. By mapping of parameter predictor the output variables are 6, forms a R^6.

```
Parameter_Predictor
// 1. MLP Forward propagation
Raw_Params ← MLP(S) // $R^7 \rightarrow R^6$
// 2. Normalization (Sigmoid)
Scaled_Params ← Sigmoid(Raw_Params)
// 3. Map to a bounded interval ($\phi$)
$\phi_{\text{scale}}$ ← Scaled_Params[0] * 1.7 + 0.3 // interaction scale ∈ [0.3, 2.0]
$\phi_{\text{power}}$ ← Scaled_Params[1] * 1.0 + 0.5 // suppression power ∈ [0.5, 1.5]
$\phi_{\text{dec1}}$ ← Scaled_Params[2] * 1.7 + 0.3 // decay modulation of $x$ net ∈ [0.3, 2.0]
$\phi_{\text{dec2}}$ ← Scaled_Params[3] * 1.7 + 0.3 // decay modulation of $y$ net ∈ [0.3, 2.0]
$\phi_{\text{exc}}$ ← Scaled_Params[4] // excitation of $y$ to $x$ ∈ [0.0, 1.0]
$\phi_{\text{inh}}$ ← Scaled_Params[5] // inhibition of $y$ of $x$ ∈ [0.0, 1.0]
Return $\phi$
```

Algorithm 1: Parameter predictor

The adaptive LSTM predictor is used to determine the inner self-adaptive mechanisms of x and y nets.

The key point is to dynamically calculate the deviation. In Algorithm 2 the input values of adaptive LSTM predictor at time t is represented by I_t, H_{t-1} represents the hidden state at time $t-1$. The accumulated deviations are represented by δ_t. The output of adaptive LSTM predictor is the predicted value P_t at time t, the contribution of deviation $\Delta\delta$, H_t. The information is used to dictate the system.

```
Adaptive_LSTM_Predictor($I_t, H_{t-1}, \mathrm{Bias}_k$)
// 1. LSTM calculation
$H_t \leftarrow$ LSTM_Core($I_t, H_{t-1}$)
$P_t \leftarrow$ Predictor_Linear($H_t$) // calibration prediction
// 2. Calculation of dynamical parameter
Features ← Concat($H_t$, $I_t$)
Base_Threshold ← Threshold_Net(Features)
Base_Weight ← Weight_Net(Features)
// 3. Application exploration bias ($\mathrm{Bias}_k$)
Dynamic_Threshold ← Base_Threshold · exp($-\mathrm{Bias}_k$)
Deviation_Weight ← Base_Weight · (1.0 + $\mathrm{Bias}_k$ · 0.5)
// 4. Calculation of contribution of deviation
$E_t \leftarrow I_t - P_t$
$|E_t| \leftarrow$ Absolute($E_t$)
// 5. Soft Mask to determine the stimulating degree
Soft_Mask ← Sigmoid(($|E_t|$ - Dynamic_Threshold) · 5.0)
// 6. Final contribution of deviation
$\Delta\delta \leftarrow E_t$ · Deviation_Weight · Soft_Mask
Return $P_t, \Delta\delta, H_t$
```

Algorithm 2: Adaptive LSTM Predictor

Though the coupling of x and y is mainly determined by Parameter_Predictor, the output of macroscopic parameters ϕ (for instance $\phi_{\text{scale}}, \phi_{\text{inh}}$), Meta_Controller in Algorithm 3 is responsible for the adaptation based on instant states. Meta_Controller accepts the instant deviations (δ_x, δ_y) of x and y and threshold information to predict the instant interaction scale and decay modulations. Its output signals, Uncertainty (uncertainty), are used to dynamically weighting the coupling terms of x and y. This makes the system's dynamics not only depending on the macroscopic environment (statistical features), but also the microscopic environment which makes the "brain" control its dynamical behavior in a refined manner.

```
Meta_Controller
// 1. input is a combined state
Combined_State ← Concat($\delta_x, \delta_y, P_x, P_y, \mathrm{Threshold}_x, \mathrm{Threshold}_y$)
// 2. Calculation of uncertainty (core signal)
Uncertainty ← Sigmoid(FNN_Uncertainty(Combined_State)) // [0, 1]
// 3. Control parameters estimation based on uncertainty
Interaction_Input ← Concat(Uncertainty, Combined_State)
Control_Params ← FNN_Interaction(Interaction_Input) // $R^4$
// 4. Mapping to control signals
Decay_$x$ ← Sigmoid(Control_Params[0]) · 0.3 + 0.01 // Instant decay modulation of $x$
$\mathrm{Interact}_x$ ← Sigmoid(Control_Params[1]) · Uncertainty // interaction scale of $x$
$\mathrm{Decay}_y$ ← Sigmoid(Control_Params[2]) · 0.3 + 0.01 // Instant decay modulation of $y$
$\mathrm{Interact}_y$ ← Sigmoid(Control_Params[3]) · (1.0 - Uncertainty · 0.5) // interaction scale of $y$
// 5. Returned Control signals
Return Decay_$x$, $\mathrm{Interact}_x, \mathrm{Decay}_y, \mathrm{Interact}_y$, Uncertainty
```

Algorithm 3: Meta Controller

The Algorithm in 4 is to exhibit in each time step t, how the macroscopic parameters ϕ to adjust the coupling of x and y and how the updating of δ. Input: I_t, Targets T_t. Variables: ϕ at time t, δ_x, δ_y (accumulated deviations) P_x, P_y (predicted calibration).

```
Unified_Coupled_System($I_t, \phi, \delta_x, \delta_y$)
// 1. LSTM prediction (By Algorithm 2)
$P_1, \Delta\delta_1, H_1 \leftarrow$ Adaptive_LSTM_Predictor($I_t$, Bias$_x$)
$P_2, \Delta\delta_2, H_2 \leftarrow$ Adaptive_LSTM_Predictor($I_t$, Bias$_y$)
// 2. Calculation of coupling term (using macroscopic parameters $\phi$)
$\phi_{\text{scale}}, \phi_{\text{power}}, \ldots, \phi_{\text{inh}} \leftarrow \phi$
// $y \rightarrow x$ signal (excitation and inhibition)
Signal$_{y\rightarrow x} \leftarrow$ Sign($\delta_y$) $\cdot$ Power($|\delta_y|$, $\phi_{\text{power}}$) $\cdot\ \phi_{\text{scale}} \cdot \phi_{\text{exc}}$ - Sign($\delta_x$) $\cdot$ Power($|\delta_x|$, $\phi_{\text{power}}$) $\cdot\ \phi_{\text{scale}} \cdot \phi_{\text{inh}}$
// cost of inhibition
Cost$_{\text{2Supp}} \leftarrow$ Absolute(Signal$_{y\rightarrow x,\text{Inh}}$) $\cdot$ 2.0
// $y \rightarrow x$ signal (difference shirk)
Signal$_{x\rightarrow y} \leftarrow \delta_x \cdot \phi_{\text{scale}} \cdot 0.1 \cdot (1.0 + \text{Capacity}_x)$
// 3. Decay of difference (Decay)
$\delta_x^{\text{decay}} \leftarrow \delta_x \cdot (x - \text{Decay}_{\text{Meta}} \cdot \phi_{\text{decx}})$ // Decay$_{\text{Meta}}$ from Algorithm 3
$\delta_y^{\text{decay}} \leftarrow \delta_y \cdot (x - \text{Decay}_{\text{Meta}} \cdot \phi_{\text{decy}})$
// 4. Updating of deviation (Key point: cost and coupling terms are added)
$\delta_x^{\text{new}} \leftarrow \delta_x^{\text{decay}} + \Delta\delta_x + \text{Signal}_{y\rightarrow x}$
$\delta_y^{\text{new}} \leftarrow \delta_y^{\text{decay}} + \Delta\delta_y + \text{Signal}_{x\rightarrow y} + \text{Cost}_{y\text{Supp}}$
// 5. Capacity limitation and punishment (hard constraint)
Penalty$_x \leftarrow$ ReLU($|\delta_x^{\text{new}}| - 0.2$)
Penalty$_y \leftarrow$ ReLU($|\delta_y^{\text{new}}| - 3.0$)
$\delta_x \leftarrow$ Clamp($\delta_x^{\text{new}}$, [-0.2, 0.2])
$\delta_y \leftarrow$ Clamp($\delta_y^{\text{new}}$, [-3.0, 3.0])
// 6. Output
Output$_x \leftarrow P_x + \delta_x$
Output$_y \leftarrow P_y + \delta_y$
Return Output$_x$, Output$_y$, Penalty$_x$, Penalty$_y$
```

Algorithm 4: Unified coupled system

The loss function (driving force of function differentiation)

In formation of key loss terms are exhibited in Table A22

Table A22: Key loss terms

Loss terms	Aim	Calculation
L_{Buffer}	Reward	Deviations of y under perturbation to buffer x.
$L_{\text{Calibration}}$	Guarantee y is calibrated baseline when there is no perturbation	$L_{\text{Calibration}} = \text{MSE}(O_2 \odot \mathbf{M}_{\text{Non-Pert}}, T \odot \mathbf{M}_{\text{Non-Pert}})$
$\mathcal{L}_{\text{Saturation}}$	punishment	deviation of x that out of capacity. $L_{\text{Saturation}} = \text{Mean}(\text{Penalty}_x)$
$\mathcal{L}_{\text{Persistence}}$	reward	persistence of y δ (negative weights).

The loss function is the key point of driving the network x and y's function differentiation. L_{Total} is the weighted addition of all loss functions. Here $\mathbf{M}_{\text{Pert}}$ is the masked perturbation. $\mathbb{I}(|I_t - T_t| > 0.1)$ and $\mathbf{M}_{\text{Non-Pert}}$ is the non-masked perturbation in which $1 - \mathbf{M}_{\text{Pert}}$ and W is the weight. The total weighted loss function is

$$L_{Total} = L_x + L_y$$

$$L_x = W_{\text{MSE}} \cdot L_{\text{MSE}}(O_1, T) + W_{\text{Sat}} \cdot L_{\text{Saturation}}$$

$$L_y = W_{\text{Buf}} \cdot L_{\text{Buffer}} + W_{\text{Cal}} \cdot L_{\text{Calibration}} + W_{\text{Inst}} \cdot L_{\text{Instability}} + W_{\text{Pers}} \cdot L_{\text{Persistence}}$$

$$L_{\text{Buffer}} = -\frac{1}{|\mathcal{T}|} \sum_{t \in \mathcal{T}} (|O_{x,t} - O_{y,t}| \cdot \mathbf{M}_{\text{Pert},t})$$

$O_{x,t}$ and $O_{y,t}$ are the output of x and y at time t. $|\mathcal{T}|$ is the total time step. $\mathbf{M}_{\text{Pert},t}$ is the masked perturbation, when $|I_t - T_t| > \theta_{\text{pert}} = 1 \quad or \quad 0$.(in our code $\theta_{\text{pert}} = 0.1$)

$$\mathcal{L}_{\text{Persistence}} = -\frac{1}{|\mathcal{T}|} \sum_{t \in \mathcal{T}} |\delta_{y,t}|$$

where $\delta_{y,t}$ is the cumulated deviations of y at time t. The weights W_{Pers} in our code is negative (-2.0), meaning that minimizing this term is equivalent to maxmize $|\delta_{y,t}|$.

Declaration of Competing Interest

None.

Declaration of generative AI in scientific writing

Authors declare no using of generative AI.

Acknowledgements

This article is dedicated to the memory of my father, Weize Lin (born 1941-07-29 – passed away 2025-05-19). His often frustrating and unpredictable behavior led me to think about the psychological causes behind it, which I came to view as similar to the reorganization of a neural network. This inspired me to model brain dynamics using artificial neural networks. Coincidentally, I later encountered relevant research that provided the data needed for this study. Unfortunately, he passed away during the course of my work. This study is a tribute to his influence on my thinking, even during a period of great personal loss.

Funding Statement

This research did not receive any specific grant from funding agencies in the public, commercial, or not-for-profit sectors.

Author contributions

Contribution of the authors: Feng Lin analyzed the data and constructed the framework, developed the analytical methodology, implemented the codes and wrote the manuscript.

Data availability

The data used in this study were originally reported by Giovanniello et al. [5] and are publicly available in their supplementary materials. The datasets used for secondary analysis can be accessed through the publication and relevant repositories, subject to any access restrictions specified by the original authors.

The computational code and models used for the Unified Coupled System (UCS) neural network simulations and the statistical robustness analysis are available from the corresponding author upon reasonable request.

Ethics Statement

This article is based on a secondary analysis of data originally reported by Giovanniello et al. [5]. As this is a secondary data analysis, no new ethical approval or animal research was conducted for this study. All experimental procedures involving animals were performed in accordance with the ethical standards established by the original study.

Statements

All authors have read and approved the final version of the manuscript. Feng Lin had access to the publicly available data used in this study and takes full responsibility for the integrity of the data analysis.

References

[1] Jamie Ward. *The student's guide to cognitive neuroscience.* Routledge, 2019.

[2] Christian A Klöckner. A comprehensive model of the psychology of environmental behaviour–a meta-analysis. *Global environmental change*, 23(5):1028–1038, 2013.

[3] Hang-Yee Chan, Maarten AS Boksem, Vinod Venkatraman, Roeland C Dietvorst, Christin Scholz, Khoi Vo, Emily B Falk, and Ale Smidts. Neural signals of video advertisement liking: Insights into psychological processes and their temporal dynamics. *Journal of Marketing Research*, 61(5):891–913, 2024.

[4] Ben Hannigan, Deborah Edwards, and Philip Burnard. Stress and stress management in clinical psychology: Findings from a systematic review. *Journal of Mental Health*, 13(3):235–245, 2004.

[5] Jacqueline R Giovanniello, Natalie Paredes, Anna Wiener, Kathia Ramírez-Armenta, Chukwuebuka Oragwam, Hanniel O Uwadia, L Yu Abigail, Kayla Lim, Jenna S Pimenta, Gabriela E Vilchez, et al. A dual-pathway architecture for stress to disrupt agency and promote habit. *Nature*, 2025.

[6] KE Kürten and JW Clark. Chaos in neural systems. *Physics Letters A*, 114(7):413–418, 1986.

[7] Christine A Skarda and Walter J Freeman. How brains make chaos in order to make sense of the world. *Behavioral and brain sciences*, 10(2):161–173, 1987.

[8] Feng Lin. Hidden complexity of biological clocks that adapt to external control and internal regulation: a case study on body temperature simulation. *Biological Rhythm Research*, 55(5-6):334–353, 2024.

[9] Geoffrey E Hinton. How neural networks learn from experience. *Scientific American*, 267(3):144–151, 1992.

[10] Vincent A Magnotta, Dan Heckel, Nancy C Andreasen, Ted Cizadlo, Patricia Westmoreland Corson, James C Ehrhardt, and William TC Yuh. Measurement of brain structures with artificial neural networks: two-and three-dimensional applications. *Radiology*, 211(3):781–790, 1999.

[11] Bokai Cao, Xiangnan Kong, and Philip S Yu. A review of heterogeneous data mining for brain disorder identification. *Brain informatics*, 2(4):253–264, 2015.

[12] David Pascucci, Maria Rubega, and Gijs Plomp. Modeling time-varying brain networks with a self-tuning optimized kalman filter. *PLoS computational biology*, 16(8):e1007566, 2020.

[13] Ted G Graber, Jong-Hee Kim, Robert W Grange, Linda K McLoon, and LaDora V Thompson. C57bl/6 life span study: age-related declines in muscle power production and contractile velocity. *Age*, 37(3):36, 2015.

[14] Don H Johnson, Sinan Sinanovic, et al. Symmetrizing the kullback-leibler distance. *IEEE Transactions on Information Theory*, 1(1):1–10, 2001.